

Linear Modes and Storm Tracks in a Two-Level Primitive Equation Model

SUKYOUNG LEE

Advanced Study Program, National Center for Atmospheric Research, Boulder, Colorado*

(Manuscript received 18 May 1993, in final form 5 May 1994)

ABSTRACT

Linear stability analyses of three-dimensional time-mean flows in a two-level primitive equation model are presented. The model's stationary wave is generated by implementing idealized mountains at the lower boundary. Two sets of experiments are performed: the first with one mountain and the second with three mountains at equal distance from each other. Structures of streamfunctions and heat fluxes from the linearly unstable normal mode are compared with their bandpass transient counterparts in the nonlinear model simulation. The three-dimensional time-mean flow, about which the equations are linearized, is convectively unstable for both the one and three mountain cases. For the three mountain case, there is reasonable agreement between the linear mode and the bandpass transient eddies in terms of both the longitudinal location of the largest eddy amplitudes and the potential enstrophy budget, suggesting that the global mode can capture the correct structure of the climatological storm tracks for different reasons. For the one mountain case, however, the largest eddy amplitude of the linear mode extends farther downstream than that of the bandpass transient eddies.

The reasonable correspondence between the linear modes and the bandpass eddies for the three mountain case appears to be due to the relative proximity of successive unstable regions. Between these successive unstable regions are diffluent flows, resulting in increased deformation and enhanced horizontal diffusion, which plays an important role in dissipating transient eddy enstrophy. It is suspected that this locally enhanced dissipation represents strained eddies by the deformation field.

1. Introduction

In the Northern Hemisphere (NH), baroclinic waves have been observed to attain their largest amplitude off the east coasts of North America and Asia (Blackmon et al. 1977). These two regions are generally referred to as storm tracks. The most commonly accepted theory that is used to account for the location of the storm tracks is the linear instability of the ultralong wavelength (7000–15 000 km) stationary waves.

In a series of papers, Frederiksen (1979a,b, 1983), Frederiksen and Bell (1987), and Frederiksen and Frederiksen (1992) showed that linear theory can indeed predict the correct geographic locations of the storm tracks. Based on a theoretical analysis of the local and global baroclinic instability of zonally varying flows in a two-layer quasigeostrophic model on a beta plane, Pierrehumbert (1984) estimates that the second-most unstable linear mode of the January three-dimen-

sional flow in Frederiksen (1983) is due to absolute instability, and hence a local mode. Here, we closely follow Pierrehumbert (1984) for definitions of absolute instability and convective instability, and local and global modes; local modes grow in situ, while global modes form in a domain with periodic boundary conditions as a wave packet passes repetitively through the same unstable zone. In a Charney model with continuous vertical shear, however, Pierrehumbert (1986) finds that absolute instability requires a negative surface zonal wind. Following this result, Lin and Pierrehumbert (1993) conclude that absolute instability of the midlatitude jets is unlikely. They suggest that if the convectively unstable mode propagates through the baroclinically unstable region slowly enough, then the mode can still grow substantially without any "recycling."

These theoretical studies tell us that there are at least three possible mechanisms for the existence of a zonally asymmetric, longitudinally confined mode: first, an absolutely unstable mode; second, a slowly propagating, convectively unstable mode; and third, a fast propagating, convectively unstable mode in a periodic domain. Both local and global modes can emerge from the first two mechanisms, but only global modes can exist from the third. All these possibilities once again raise the question of what physical mechanism is responsible for generating linear

* The National Center for Atmospheric Research is sponsored by the National Science Foundation.

Corresponding author address: Dr. Sukyoung Lee, Department of Meteorology, The Pennsylvania State University, 503 Walker Building, University Park, PA 16802.

storm track modes, such as presented in Frederiksen (1979a,b, 1983), Frederiksen and Bell (1987), and Frederiksen and Frederiksen (1992). In these studies, the zonally inhomogeneous flows of which linear instability analyses were performed are either idealized long planetary waves with zonal wavenumbers 3 and 4 or the observed stationary wave. When the zonal wavenumber of the stationary wave is larger than one, regional linear modes are also found that are equidistant from the upstream local baroclinicity maximum and the downstream local baroclinicity minimum. For reasons that will be explained later, it is unclear whether the linear modes examined in the above studies are local or global. As Pierrehumbert (1984) points out, one needs to be careful in interpreting linear stability calculations of a zonally inhomogeneous flow because global modes may have different physical consequences than local modes.

A physical interpretation of a global mode is more complex than that for a local mode. As a natural extension of a baroclinic wave life cycle in a zonally symmetric atmosphere (Simmons and Hoskins 1978; Randel and Stanford 1985; Feldstein and Held 1989), it is plausible that the local mode can explain local growth of baroclinic waves in the upstream end of the storm track as a part of the life cycle, which is followed by barotropic decay downstream of the storm track. In light of our ample experience with baroclinic normal mode theory, the life cycle picture described above involving the local mode is rather "intuitively" expected. Global modes can be relevant for the storm track when a large number of them interfere constructively to represent the transient evolution of a wave packet (Whitaker and Barcilon 1992), although there is no reason for any arbitrary perturbation to project into global modes that interfere constructively in the storm track region, unless the initial perturbation already has a wave packet structure as in Whitaker and Barcilon. However, when a single unstable mode is considered, even the possibility of constructive interference is eliminated. Because this global mode owes its existence to the periodic boundary condition of the domain, it usually takes a long time to emerge into the normal mode structure from an arbitrary initial perturbation, and therefore a single global mode seems to be irrelevant for the storm tracks. Therefore, it is important to identify whether an unstable mode is local or global. In the latter case, any good agreement between a single linear mode with the nature's storm track is likely to be fortuitous.

In this paper, our primary aim is to address the interpretation of the unstable modes in a zonally inhomogeneous background flow. Specifically, we examine an idealized model atmosphere in which all unstable modes are convectively unstable to show that a global mode can agree reasonably well with the model's nonlinear storm track simply because the length of the unstable region is small. The resulting fortuitous agreement can also be illustrated by ex-

amining a global mode in a model atmosphere with greater length to the unstable region. This study, however, is not to determine if the unstable linear modes, found by others (e.g., Frederiksen 1983; Robertson and Metz 1989) using the observed basic state, are local or global, but to emphasize that caution is needed in interpreting a linear mode that resembles climatological storm tracks. At present, it remains unknown as to whether the atmosphere is convectively or absolutely unstable.

If the atmosphere does not support any absolutely unstable modes or slowly propagating convectively unstable modes (Lin and Pierrehumbert 1993), what would be the possible mechanisms responsible for the geographically localized nonlinear storm track? One possibility is the Type B cyclogenesis (Petterssen and Smebye 1971), which was also illustrated using a linear superposition of a large number of global modes by Whitaker and Barcilon (1992). They showed that many global modes can interfere to form a localized storm track in a region where the surface friction is weaker and static stability is smaller. Chang and Orlanski (1993), using a convectively unstable time-mean flow, show that storm tracks can come to an end by locally enhanced surface friction. Without the stronger surface friction, the storm tracks can extend farther downstream due to downstream development. In both studies, the zonally varying surface friction, which mimics the boundary condition of land-sea distribution in the atmosphere, plays an important role.

In addition to the zonally varying surface friction or static stability, horizontal deformation can also play a role in reducing the amplitude of linear and observed storm tracks: In observational studies (Dole 1986; Mullen 1987; Lau 1988), it is clearly shown that the stationary ridge downstream of the major two oceanic storm tracks plays an important role in terminating storm tracks. Robertson and Metz (1989) performed three-dimensional linear stability analyses of the European Centre for Medium-Range Weather Forecasts analyzed winter climatology, as well as of large-scale persistent flow anomalies such as the Pacific/North American (PNA), east Atlantic (EA), and North Atlantic oscillation (NAO) patterns. For the negative PNA basic state where the stationary eastern Pacific ridge is strongest among the six phases of the persistent flow anomalies, both the "linear Pacific storm track," obtained from the fastest-growing normal mode, and the observed storm track are sharply terminated just upstream of the stationary ridge. This results in an excellent agreement between the linear and observed storm track structure (see Figs. 12d, f, and 13b of Robertson and Metz). However, for other cases (climatology, +PNA, -EA, +NAO, and -NAO) where the quasi-stationary ridge is weaker than that of the -PNA, the maximum of the linear Pacific storm track lies as much as 30 degrees downstream of the observed Pacific

storm track; the observed storm tracks tend to terminate upstream of the stationary ridge as in the -PNA case, but the linear storm track often extends farther eastward. Therefore, it appears that the downstream ridge plays an important role in zonally localizing both linear and climatological storm tracks, with the former being more sensitive to the strength of the downstream ridge. We also point out that most of the models used in the linear stability studies [e.g., Frederiksen (1983) and Robertson and Metz (1989), among others] do not include zonally varying surface friction, diabatic heating, or static stability in their linearized equations. These effects are implicitly included in their basic states.

It is a natural question then to ask how the wave activity amplitude decreases due to the stationary ridge. As mentioned earlier, this stationary ridge produces a deformation field. Shutts (1983) shows that eddies embedded within deformation fields are strained into filaments. One may suspect then that downscale enstrophy cascade occurs as this process progresses. The tendency of the observed storm tracks to terminate just upstream of the deformation field associated with the stationary ridge, as noted earlier, further supports this conjecture. Therefore, our second aim of this paper is to investigate the role of dissipation through enstrophy cascade toward small scales in the formation of the model's zonally localized storm track.

The model description and design of the experiment is described in section 2. Stationary waves and climatological transient eddy statistics are presented in section 3. In section 4, we discuss the results of the linear stability analysis. The diagnosis of the storm track is described in section 5. Concluding remarks follow in section 6.

2. Model description and design of experiment

a. Model description

Without idealized mountains, the model we used here is identical to the two-level primitive equation model in Lee and Held (1993). The horizontal resolution of the model is R30, and two vertical levels in pressure coordinates are used. We assume that the presence of a "mountain" results in a prescribed pressure distribution $P_B(\lambda, \phi)$ at the surface, with λ and ϕ being longitude and latitude, respectively. In other words, this prescribed pressure distribution accounts for the change in surface pressure following the mountain surface. As we will see in (5), this boundary pressure distribution results in a boundary condition analogous to that typically used in height coordinates. In the absence of the mountain, the value of P_B would have a constant value of 1000 mb. The pressure difference between the surface and 500 mb is

$$\Delta P_2(\lambda, \phi) = \Delta P - P_B(\lambda, \phi), \quad (1)$$

where ΔP (=500 mb) is the vertical pressure difference between the full levels.

The continuity equation,

$$\nabla \cdot \mathbf{u} + \frac{\partial \omega}{\partial P} = 0, \quad (2)$$

where $\mathbf{u} = (u, v)$ being the horizontal velocity, gives equations for mass conservation at each level:

$$D_1 \Delta P = -\omega_M \quad (3a)$$

$$D_2 \Delta P_2(\lambda, \phi) = \omega_M - \omega_B, \quad (3b)$$

where D_i is the divergence in either layer; ω_M and ω_B are the vertical velocities at 500 mb and at the lower boundary, respectively. The vertical velocity at the upper boundary is set to zero. Subscripts 1 and 2 refer to the upper and lower levels, respectively. By substituting (1) into (3b), and adding equations (3a) and (3b), we obtain

$$D_1 \Delta P + D_2(\Delta P - P_B(\lambda, \phi)) = -\omega_B. \quad (4)$$

The vertical velocity at the surface is

$$\omega_B = \frac{dP_B(\lambda, \phi)}{dt} = -\mathbf{u}_2 \cdot \nabla P_B(\lambda, \phi), \quad (5)$$

where we assume that $\omega = 0$ at the lower boundary in the absence of the mountain. This is analogous to the boundary condition $w = \mathbf{u} \cdot \nabla h(\lambda, \phi)$, where w is the vertical velocity and h is the mountain height in standard height coordinates.

After substituting (5) into (4), and rearranging terms, (4) can be rewritten as

$$\begin{aligned} (D_1 + D_2) \Delta P &= D_2 P_B(\lambda, \phi) + \mathbf{u}_2 \cdot \nabla P_B(\lambda, \phi) \\ &= \nabla \cdot [P_B(\lambda, \phi) \mathbf{u}_2]. \end{aligned} \quad (6)$$

Thus, the vertically averaged divergence source due to the flow over the mountain is of the form

$$D_{\text{topo}} \equiv \frac{D_1 + D_2}{2} = \frac{\nabla \cdot [P_B(\lambda, \phi) \mathbf{u}_2]}{2 \Delta P}. \quad (7)$$

After defining the variables

$$\mathbf{u}_b = \frac{\mathbf{u}_1 + \mathbf{u}_2}{2}$$

and

$$\mathbf{u}_c = \frac{\mathbf{u}_1 - \mathbf{u}_2}{2},$$

the two-level primitive equation model that includes idealized mountains can then be written as

$$\frac{\partial \zeta_b}{\partial t} = -\nabla \cdot [(f + \zeta_b)\mathbf{u}_b + \zeta_c \mathbf{u}_c] - \frac{1}{2} \nabla \times [P_p(D_{\text{topo}} + D_c)\mathbf{u}_c] - \frac{\kappa_2}{2} \zeta_b + \frac{\kappa_2}{2} \zeta_c - \nu \left(\frac{2}{\alpha^2} + \nabla^2 \right)^4 \zeta_b, \quad (8a)$$

$$\frac{\partial \zeta_c}{\partial t} = -\nabla \cdot [(f + \zeta_b)\mathbf{u}_c + \zeta_c \mathbf{u}_b] - \frac{1}{2} \nabla \times [P_m(D_{\text{topo}} + D_c)\mathbf{u}_c] + \frac{\kappa_2}{2} \zeta_b - \frac{\kappa_2}{2} \zeta_c - \nu \left(\frac{2}{\alpha^2} + \nabla^2 \right)^4 \zeta_c, \quad (8b)$$

$$\begin{aligned} \frac{\partial D_c}{\partial t} = & \nabla \times [(f + \zeta_b)\mathbf{u}_c + \zeta_c \mathbf{u}_b] - C_p B \nabla^2 \Theta_b - \nabla^2 E_c \\ & - \frac{1}{2} \nabla \cdot [P_m(D_{\text{topo}} + D_c)\mathbf{u}_c] + \frac{\kappa_2}{2} (D_{\text{topo}} - D_c) - \nu \left(\frac{2}{\alpha^2} + \nabla^2 \right)^4 D_c, \quad (8c) \end{aligned}$$

$$\frac{\partial \Theta_b}{\partial t} = \nabla \cdot [\Theta_b \mathbf{u}_b] + \Theta_b D_{\text{topo}} - \frac{1}{2} P_p \Theta_c (D_{\text{topo}} + D_c) - r(\Theta_b - \Theta_e) - \nu \nabla^8 \Theta_b, \quad (8d)$$

where

$$\zeta = \nabla \times \mathbf{u}, \quad D = \nabla \cdot \mathbf{u}, \quad E_c = \mathbf{u}_b \cdot \mathbf{u}_c,$$

and

$$B = \frac{1}{2} \left[\left(\frac{P_2}{P_s} \right)^\kappa - \left(\frac{P_1}{P_s} \right)^\kappa \right] = 0.124,$$

with $\kappa = 2/7$. In (8), the effect of mountains is incorporated through P_p and P_m :

$$P_p(\lambda, \phi) = 1 + \frac{\Delta P}{\Delta P_2}, \quad (9a)$$

$$P_m(\lambda, \phi) = 1 - \frac{\Delta P}{\Delta P_2}. \quad (9b)$$

When $P_B(\lambda, \phi) = 0$, $P_p = 2$ and $P_m = 0$. If these values are substituted into (8), equations with the uniform boundary condition [(2a-d) in Lee and Held (1993)] are recovered.

As one can see by comparing (8a-d) with (1) of Hendon (1986), our "mountain" is implemented differently from his. In Hendon, it is assumed that the surface pressure on the mountain is 1000 mb, the same as the surface pressure in the plains, and only the model's lower layer "feels" the mountain effect mimicked by an appropriate vorticity and divergence forcing. In this aspect, the way we treat the mountain seems more physical. However, the shortcoming of our approach is that the mountain cannot be higher than 2 km in this pressure coordinate two-level model. This problem can be resolved by using a sigma coordinate model, but this takes away a number of simplicities. The resulting weak stationary wave amplitude clearly limits this model's ability to simulate stationary waves with realistic amplitude. The model is further simplified so that surface friction and static stability is uniform over

the entire globe. Once again, these idealizations make any comprehensive study of storm tracks impossible. However, we believe that these limitations do not hinder us from testing our hypothesis mentioned in section 1.

We fix the value that represents static stability, Θ_e , as 15 K. The value of Θ_e is

$$\Theta_e = \frac{\Theta_m}{3} (1 - 3 \sin^2 \phi), \quad (10)$$

where Θ_m is the temperature difference between the pole and equator in radiative equilibrium. The value of Θ_m is chosen as 80 K. The radiative relaxation time-scale r^{-1} is 30 days. Only the lower-level wind feels mechanical damping with the value of the coefficient κ_2 being 0.2 day⁻¹. The coefficient of the quadharmonic horizontal diffusion ν is chosen as 8×10^{38} m⁸ s⁻¹. For a few selected calculations, we also use a smaller value for ν (8×10^{37} m⁸ s⁻¹).

b. Experimental design

To examine the sensitivity of the linear theory to the zonal wavenumber of the stationary wave, we integrate the model both with one mountain and with three mountains. We refer to the cases for one and three mountains as M1 and M3. For the latter case, the mountains are 120 degrees apart from each other. The M3 case is chosen to resemble the wavenumber 3 structure of the stationary wintertime NH circulation.

The shape of the mountain is Gaussian:

$$P_B(\lambda, \phi) = P_0 \exp \left[\left(\frac{\lambda - 60^\circ}{15^\circ} \right)^2 + \left(\frac{\phi - 45^\circ \text{N}}{15^\circ} \right)^2 \right]. \quad (11a)$$

and

$$P_B(\lambda, \phi) = P_0 \exp \left[\left(\frac{\lambda - 60^\circ}{15^\circ} \right)^2 + \left(\frac{\phi - 45^\circ\text{N}}{15^\circ} \right)^2 \right] + P_0 \exp \left[\left(\frac{\lambda - 180^\circ}{15^\circ} \right)^2 + \left(\frac{\phi - 45^\circ\text{N}}{15^\circ} \right)^2 \right] + P_0 \exp \left[\left(\frac{\lambda - 300^\circ}{15^\circ} \right)^2 + \left(\frac{\phi - 45^\circ\text{N}}{15^\circ} \right)^2 \right] \quad (11b)$$

for the M1 and M3 cases, respectively. The height of the mountain P_0 is 200 mb. This value corresponds to approximately 2 km in height. Figure 1 shows the structure of P_h for both the M1 and M3 cases.

3. Model simulations and analysis

a. Stationary waves

The horizontal structure of the 4000-day average zonal wind at the upper level for the M1 case is shown in Fig. 2a. A well-defined jet stream lies about 60 degrees downstream of the mountain with its maximum wind speed of 50 m s^{-1} .

In Fig. 3a, we show the time-mean zonal wind at the upper level for the M3 case. In this case, there are three well-defined jet streams of 44 m s^{-1} , located about 60 degrees downstream of the corresponding mountains, showing a clear wavenumber 3 structure. The value of the zonal-mean zonal wind at the upper level is essentially identical ($\sim 36 \text{ m s}^{-1}$) for both M1 and M3 cases, yet the value of the jet maximum is smaller for the M3 than that for the M1 case.

For both cases, the streamfunction field (Figs. 2b and 3b) indicates that the amplitude of the stationary wave is smaller than that in the typical Northern Hemisphere winter circulation, particularly near the Rocky Mountains. This may be, among other reasons, at least partially due to the smaller height of the mountain and the lack of land-sea temperature contrast in the model.

In both observations and models (e.g., Blackmon et al. 1977; Kushnir and Esbensen 1986a), there has been evidence that storm tracks are closely related with the baroclinicity of the time-mean flow. Because the two-level model is used in this study, it is convenient to measure the baroclinicity of the time-mean flow by the linear growth rate of Phillips' two-layer model. Then the form of the baroclinicity parameter is

$$\sigma = \frac{k \{ 4K^4 U_c^2 (L^{-4} - K^4) - \beta^2 L^{-4} \}^{1/2}}{2K^2 (L^{-2} + K^2)}, \quad (12)$$

where $K^2 = k^2 + l^2$ with k and l being zonal and meridional wavenumbers, respectively, $U_c = (U_1 - U_2)/2$, and L is the internal Rossby radius of deformation. With values of $k = 1.2 \times 10^{-6} \text{ m}^{-1}$, $l = 3 \times 10^{-6} \text{ m}^{-1}$, and $L^{-1} = 1.4 \times 10^{-6} \text{ m}^{-1}$, the baroclinicity parameter is shown in Fig. 2c and Fig. 3c for the M1 and M3 cases. The maxima of baroclinicity lies slightly pole-

ward and eastward of the vertical wind shear maxima (not shown). The maximum value of σ is about $1/6 \text{ day}^{-1}$.

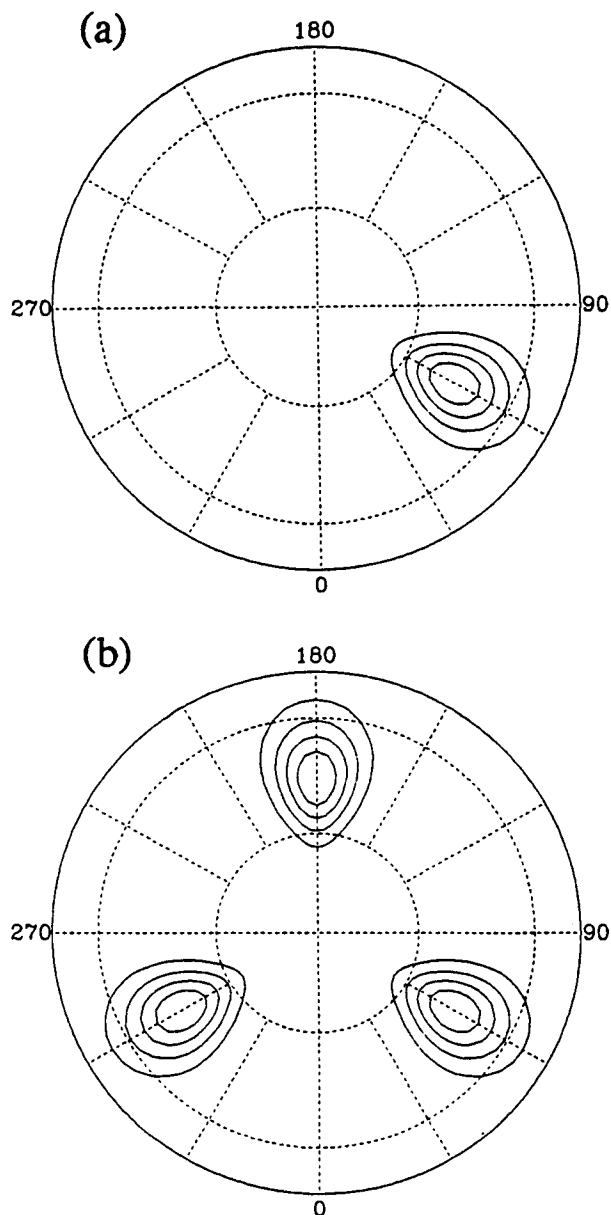
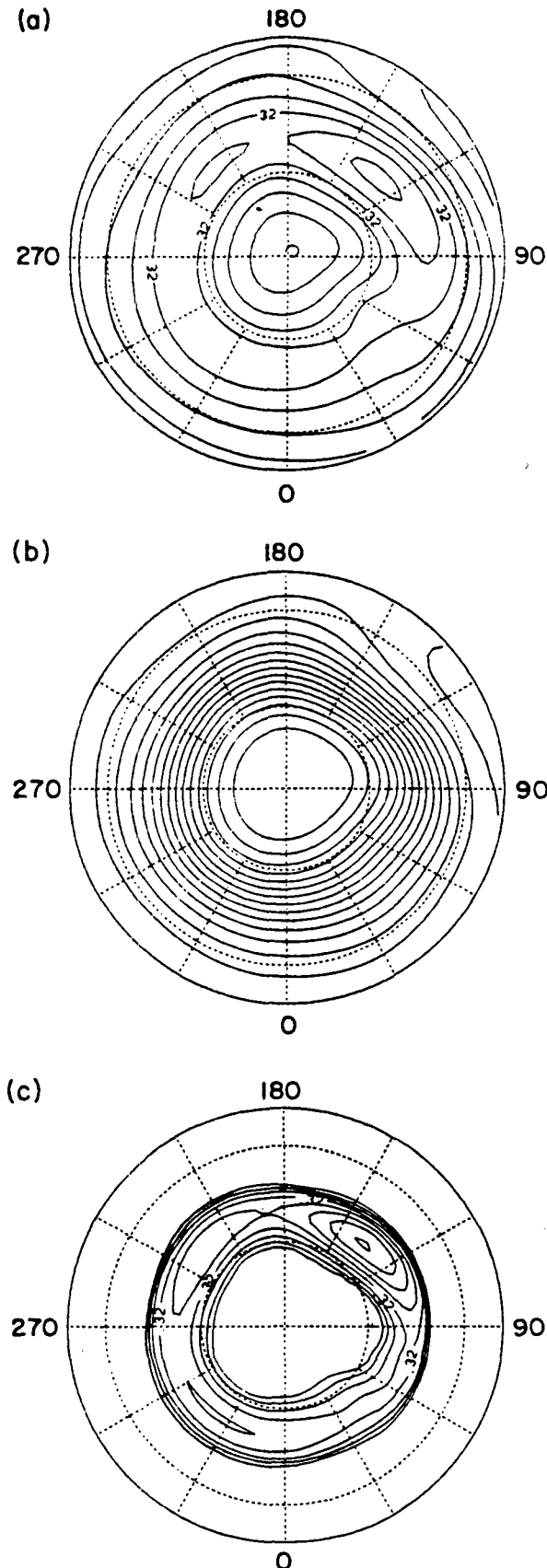


FIG. 1. Structure of mountains for (a) M1 and (b) M3 cases. Contour interval is 40 mb. The outmost circle represents 20°N .



b. Transient eddy statistics

The transient eddies are bandpass filtered at a period of 2–6 days. The bandpass upper-level streamfunction variance ($\overline{\psi_1'^2}$) and the vertically averaged heat flux ($\overline{v_b' T_b'}$) are shown in Figs. 4 and 5 for the M1 and M3 cases. The overbar refers to the time mean, and the prime to the bandpass eddies. We define the storm track region where the value of high-frequency variance or covariance is greater than 80% of the maximum value in the domain, and indicate the region by shading. We chose this criteria because it separates the Pacific storm track from the Atlantic storm track fairly well in observations (e.g., see Blackmon et al. 1977).

For the M1 case, the maximum in the upper-level streamfunction variance (Fig. 4a) lies 30 degrees downstream of the jet center. The lower-level streamfunction variance also peaks at the same location (not shown). The maximum poleward heat flux (Fig. 4b) occurs slightly upstream of the corresponding streamfunction variance maximum and downstream of the enhanced baroclinicity region (Fig. 2c).

The streamfunction variance for the M3 case is shown in Fig. 5a. The local maximum in the streamfunction variance, which appears downstream of the mountain that lies in the same location as the single mountain in the M1 case, is indicated by A. The other two storm tracks lie 120 degrees apart from one another, consistent with the distance between the mountains. Although the storm tracks in the M3 case (in particular, see the region indicated by A in Fig. 5a) tend to lie slightly upstream of the storm track in the M1 case (Fig. 4), the location of the model's storm track measured by the streamfunction variance shows very small sensitivity to the number of the mountains in the domain. However, the storm tracks for the M3 case have smaller (10%) amplitude than the storm track for the M1 case.

As for the M1 case, the streamfunction variance (Fig. 5a) maxima are associated with the local poleward heat flux maximum (Fig. 5b) and the maximum baroclinicity (Fig. 3c). This suggests that the bandpass eddies in the storm tracks are associated with active baroclinic processes east of the mountain. These qualitative features of transient eddy statistics resemble both observations (Blackmon et al. 1977) and more realistic model results (e.g., Kushnir and Esbensen 1986a).

4. Linear stability analysis

In this section, we examine the linear stability of the three-dimensional stationary waves. To obtain growth rate, frequency, and structure of the unstable normal

FIG. 2. Time-mean flow for the M1 case: (a) upper-level zonal wind, (b) upper-level streamfunction, and (c) baroclinicity parameter. Contour intervals are (a) 8 m s^{-1} , (b) $10^7 \text{ m}^2 \text{ s}^{-1}$, and (c) 0.1 day^{-1} .

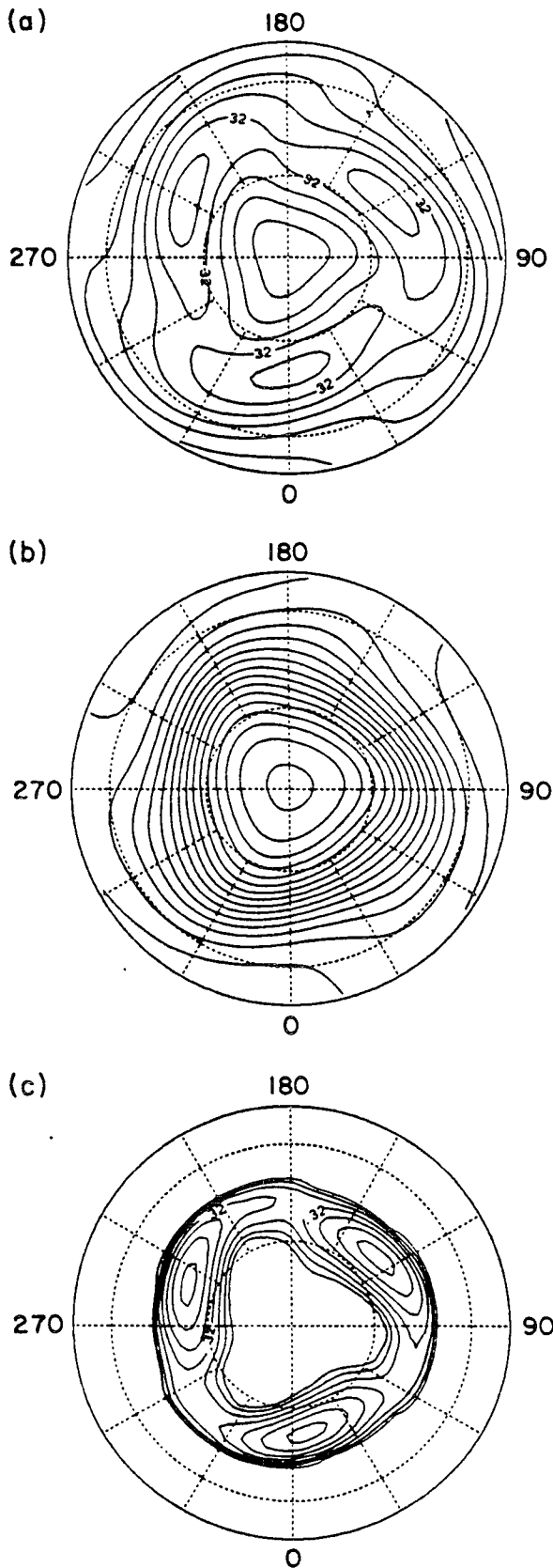


FIG. 3. As in Fig. 2 except for the M3 case.

modes, we solve the matrix eigenvalue–eigenvector problem.

To generate the matrix, of which eigenvalues and eigenvectors are sought, we first linearize the four prediction equations (8a–d) about the time-mean state. Then we perturb one spectral coefficient at a time and use the linearized model to calculate the time tendency. The resulting tendency terms give a column of the coefficient matrix. After the complete coefficient matrix is obtained, we solved for the eigenvalues and eigenvectors of the time-mean basic state using an EISPACK routine for a general complex eigensystem. For an R30 truncation, the resulting size of the matrix is too large

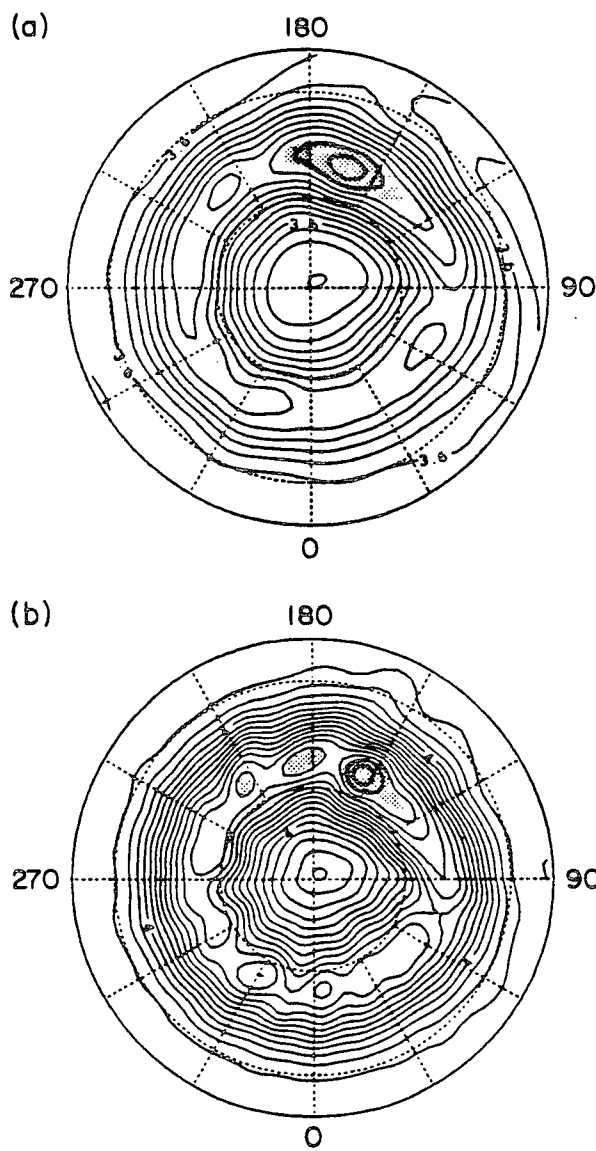


FIG. 4. Bandpass filtered (a) variance of the upper-level streamfunction and (b) poleward heat flux for the M1 case. Contour intervals are (a) $9 \times 10^{12} \text{ m}^4 \text{ s}^{-2}$ and (b) 1 km s^{-1} . Shading denotes values greater than 80% of the maximum.

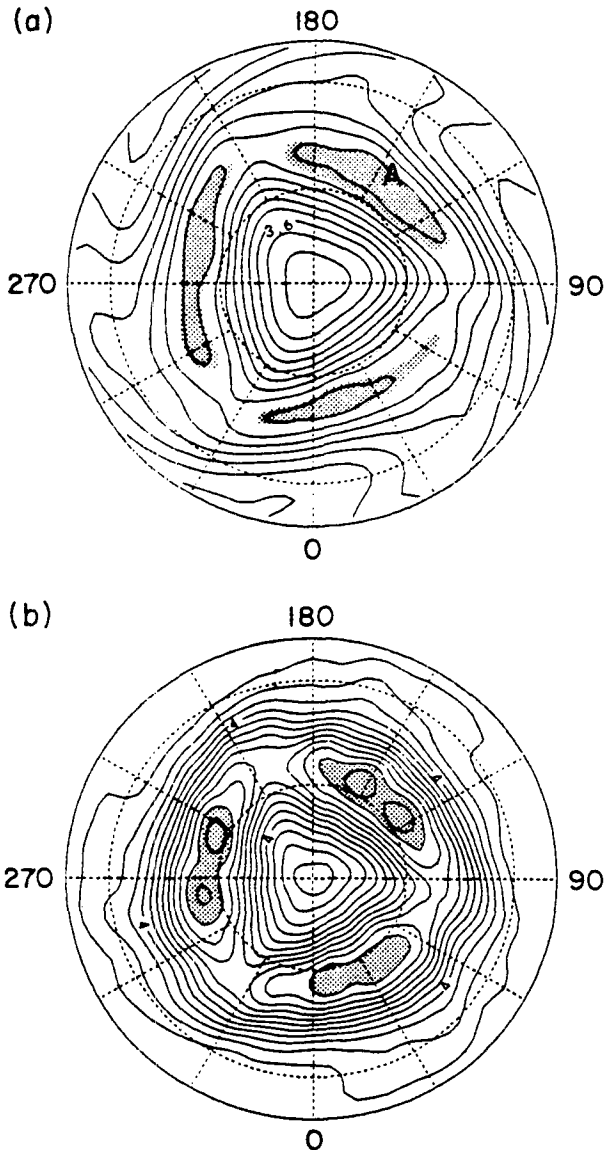


FIG. 5. As in Fig. 4 except for the M3 case. See text for explanation of the letter A.

to handle with the given memory of the computer. Thus, we decided to retain wavenumbers corresponding to an R15 truncation. We also checked the most unstable linear normal mode of the stationary wave calculated by the eigenvalue–eigenvector method against that obtained by an initial value problem of the linearized model. This initial value problem, which only calculates the fastest-growing mode, does not require a large amount of memory, so we repeated the same calculation for the R30 version of the linear model. This enables us to check the sensitivity of the most unstable eigenmode against the resolution of the model. To further test the robustness of the mode, we repeated the same calculation once again, with a value of the quad-

TABLE 1. Linear stability analysis for the M1 case.

Resolution of linear model	Growth rate ω_i (day ⁻¹)	Frequency ω_r (day ⁻¹)
R30	0.266	3.30
R15	0.301	3.15
R15	0.299	3.16
R15	0.282	2.62
R15	0.273	2.62
R15	0.267	3.68

harmonic diffusion coefficient of 8×10^{37} instead of 8×10^{38} , fixing the resolution of the model at R30.

For both M1 and M3 cases, there are many (~ 20) unstable modes. Growth rate, phase speed, and dominant zonal wavenumber for the five most unstable linear normal modes (mode 1–mode 5 hereafter), computed by the eigenvalue problem with the R15 truncation, are listed in Tables 1 and 2. Also listed is the most unstable linear mode (mode 1/R30) obtained from the initial value problem for the R30 truncation. Although the growth rate of mode 1 is approximately 10% greater than that of mode 1/R30, the frequencies agree well with each other. As will be shown later, the structure of mode 1 is essentially identical to that for mode 1/R30 in both cases. The period of these modes is between 2 and 3 days, which is consistent with the characteristics of the “cyclogenesis mode” in Frederiksen and Bell (1987) and in Robertson and Metz (1989). The discrepancy between the growth rates between mode 1/R30 and mode 1 is at least partly due to the scale-selective horizontal diffusion, whose dissipative effect is stronger in the presence of the higher harmonics in the R30 model.

Figure 6a shows the upper-level streamfunction of mode 1 for the M1 case. The zonal scale of the mode is dominated by wavenumber 6. The ambiguity of the phase can be removed in bilinear quantities, such as streamfunction variance and heat fluxes, by performing the random phase ensemble average (RPEA), which is essentially an average over the intrinsic period of the normal mode, as described in Frederiksen (1983). The RPEA streamfunction variance at the upper level, $\{\psi_1^{\prime 2}\}$, is shown in Fig. 6b where the braces denote RPEA. To compare the structure of the linear mode with the climatological storm track of the model, we

TABLE 2. Linear stability analysis for the M3 case.

Resolution of linear model	Growth rate ω_i (day ⁻¹)	Frequency ω_r (day ⁻¹)
R30	0.190	3.10
R15	0.223	2.63
R15	0.217	2.63
R15	0.216	3.16
R15	0.213	3.07
R15	0.189	2.10

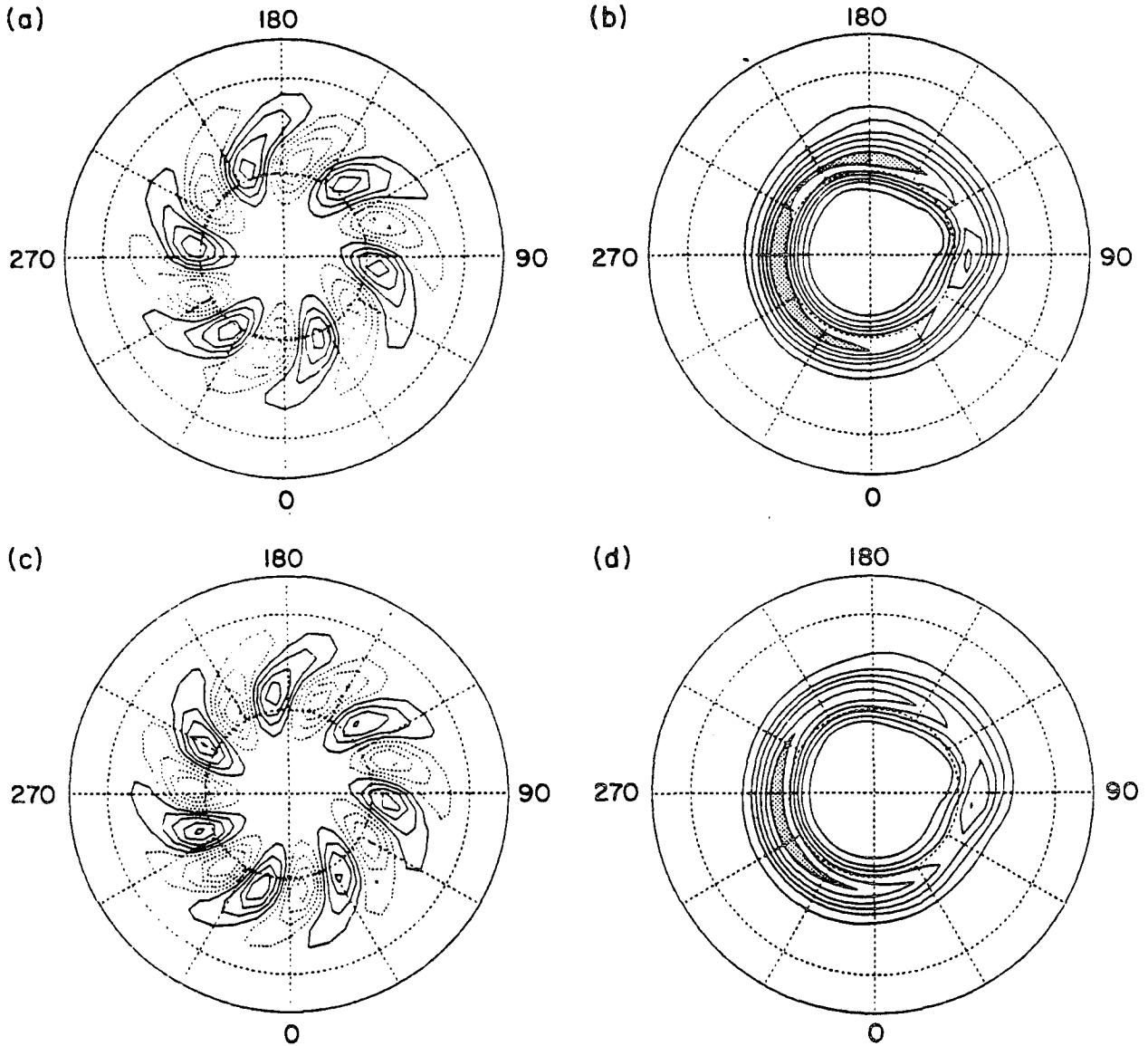


FIG. 6. Linear stability analysis for the M1 case: (a) upper-level streamfunction and (b) RPEA upper-level streamfunction for the most unstable mode (mode 1); (c) and (d) are the same as (a) and (b), respectively, except for the third most unstable mode (mode 3). Contour interval is arbitrary.

define the storm tracks of the linear mode as regions where the amplitude of the RPEA variance is greater than 80% of its maximum, and these regions are indicated by shading. In Fig. 7a, we show $\{\psi_1^{\prime 2}\}$ for mode 1/R30, which is essentially identical with $\{\psi_1^{\prime 2}\}$ for mode 1 (Fig. 6b). We do not show it here, but the structure as well as growth rate and frequency of the most unstable mode obtained with an order of magnitude smaller value of the diffusion coefficient in the R30 linear model also agrees well with that for mode 1/R30. Therefore, we believe that the most unstable mode obtained using the eigenvalue problem is robust.

We now proceed to compare the results of linear stability analyses with the climatological storm tracks

of the model. We first consider results for the M1 case. The zonal scale of the "linear storm track" (Fig. 7a) is far greater than that of the bandpass transient eddies (Fig. 4a) as the downstream end of the linear storm track lies at $\lambda = 30^\circ$, only about 30° upstream of the mountain. The vertically averaged RPEA heat flux (Fig. 7b) shows essentially the identical structure. The same is true for the lower-level RPEA streamfunction variance (not shown). The structure of mode 2 is very similar to mode 1. The upper-level streamfunction and the RPEA upper-level streamfunction variance for mode 3 is shown in Figs. 6c and 6d. The zonal scale peaks at wavenumber 7, and at the same time the perturbations lie slightly equatorward of mode 1 (Fig. 6a).

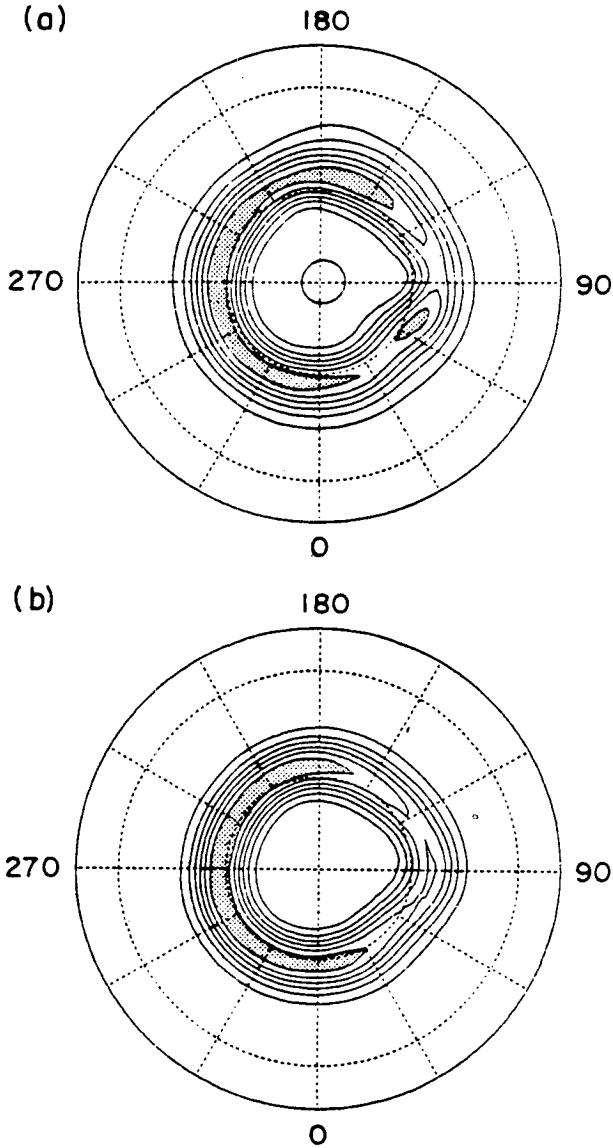


FIG. 7. Linear stability analysis for the M1 case: RPEA (a) streamfunction and (b) vertically averaged poleward heat flux of the most unstable mode, obtained by an initial value problem for the R30 truncation (mode 1/R30).

Once again, however, the mode 3 storm track lies downstream of the climatological storm track. We examined other unstable modes but none of these resemble the climatological storm track.

Figure 8 shows the RPEA variances of the mode 1/R30 for the M3 case. In this case, where the zonal wavenumber of the stationary wave is three instead of one, the linear storm track as measured by RPEA streamfunction, and heat flux agrees with the climatological storm tracks reasonably well (compare with Fig. 5) in longitude, although the former lies slightly poleward and downstream of the latter. We also investigated the other unstable modes from the eigenvalue

analyses and found that the cyclogenesis modes, including the first six fastest-growing modes, exhibit the same characteristics. The central result is that the RPEA of the linear modes agrees reasonably well with the bandpass transient eddy statistics for the M3 case but not for the M1 case.

It is a natural question, as stated in section 1, to ask whether the good agreement between the linear mode and climatological storm track for the M3 case is accidental, or if the time-mean states for the M1 and M3 cases possess different properties, resulting in different linear modes. To explore these possibilities, we further examine the linear instability properties of each time-mean flow.

To determine if the time-mean flow is absolutely unstable, we integrate the linearized model starting with

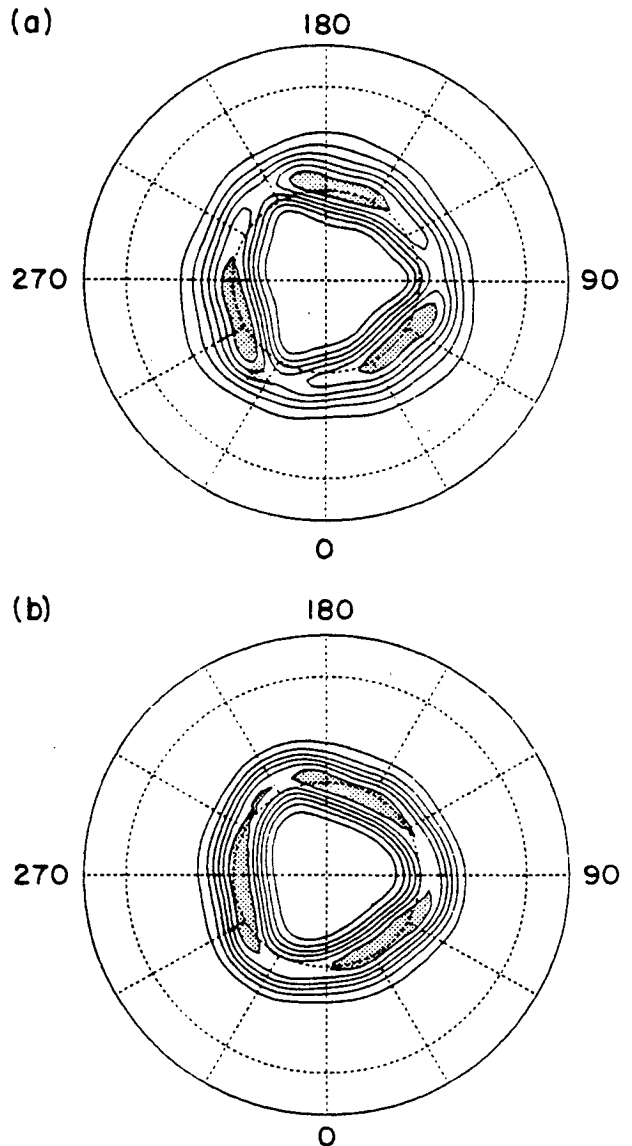


FIG. 8. As in Fig. 7 except for the M3 case.

an arbitrary small disturbance in the most unstable region ($120 \leq \lambda \leq 150$) of the domain. In Fig. 9, we show the first 10 days of the initial evolution for the M1 case. We used several different random initial conditions, and this is a typical result. The contour interval used remains the same for the entire 10-day period. As the disturbance grows, it also propagates eastward. By day 5 (Fig. 9e), the disturbance stops growing in the unstable region as the growing part of the disturbance moves completely out of that region. The disturbance propagates continuously downstream until it reenters the unstable region at day 10. The normal mode structure starts to emerge approximately at day 50 (not shown). This clearly indicates that the basic state is convectively unstable, and the linear mode shown in Fig. 7 is global. Figure 10 shows the same initial evolution as Fig. 9 but for the M3 case. Essentially identical results are found for the M3 case as well.

5. Enstrophy budget

Given the fact that the most unstable linear mode is convectively unstable, it is of interest to understand the mechanism that determines the zonal scale of both the climatological and linear storm tracks in the model. In particular, as mentioned in the introduction of this paper, we focus on the role of diffusive dissipation on the zonal scale of the storm track. As a diagnostic tool, the eddy potential enstrophy equation seems to be a natural choice for this purpose.

We consider the quasigeostrophic potential vorticity equation for the two-layer system:

$$\frac{Dq_1}{Dt} = r \frac{f_0}{\Theta_c} \Theta_b - \nu \nabla^8 q_1 \quad (13a)$$

$$\frac{Dq_2}{Dt} = -r \frac{f_0}{\Theta_c} \Theta_b - \kappa_2 \zeta_2 - \nu \nabla^8 q_2, \quad (13b)$$

where

$$q_i = f_0 + \zeta_i + (-1)^i \frac{f_0}{\Theta_c} \Theta_b, \quad i = 1, 2$$

with subscripts 1 and 2 representing the upper and lower levels, respectively. Decomposing each variable into time mean, bandpass filtered, and remainder of the two (denoted by tilde) and linearizing (13) about the time-mean state, we obtain

$$\begin{aligned} \frac{\partial q_i'}{\partial t} + \bar{\mathbf{u}}_i \cdot \nabla q_i' &= \mathbf{u}_i' \cdot \nabla \bar{q}_i \\ &- (\mathbf{u}_i' \cdot \nabla \bar{q}_i + \mathbf{u}_i' \cdot \nabla q_i' + \tilde{\mathbf{u}}_i \cdot \nabla \bar{q}_i + \tilde{\mathbf{u}}_i \cdot \nabla q_i') \\ &- (-1)^i r \frac{f_0}{\Theta_c} \Theta_b' - \nu \nabla^8 q_i', \quad (14) \end{aligned}$$

where $q_i = \bar{q}_i + \tilde{q}_i + q_i'$, $i = 1, 2$; the tilde denotes low-frequency transients. Multiplying (14) by q_i' and averaging in time, one obtains the eddy potential enstrophy equations:

$$\begin{aligned} \frac{\partial e_i}{\partial t} + \bar{\mathbf{u}}_i \cdot \nabla e_i &= - \overline{\mathbf{u}_i' q_i' \cdot \nabla \bar{q}_i} - \overline{q_i' (\mathbf{u}_i' \cdot \nabla \tilde{q}_i + \mathbf{u}_i' \cdot \nabla q_i' + \tilde{\mathbf{u}}_i \cdot \nabla \bar{q}_i + \tilde{\mathbf{u}}_i \cdot \nabla q_i')} \\ &- (-1)^i r \frac{f_0}{\Theta_c} \overline{q_i' \Theta_b'} - \overline{\nu q_i' \nabla^8 q_i'} - \delta_{i,2} \kappa_2 \overline{q_i' \zeta_2'}, \quad (15) \end{aligned}$$

where $e_i = \overline{q_i'^2}/2$. For a sufficiently long time integration, the local tendency term on the lhs of (15) vanishes. Thus, the sum of all terms on the rhs of (15) (R hereafter) should be equal to advection of the eddy potential enstrophy by the time-mean flow [second term on the lhs of (15)]. It turns out that the balance is reasonably good except near the mountain, where the ageostrophic flow becomes important.

Figure 11a shows the eddy potential enstrophy at the upper level, $q_1'^2$ for the M1 case. The maximum $q_1'^2$ lies slightly downstream of the eddy streamfunction maximum, suggesting that the eddy scale is smaller in that region. As shown in Fig. 11b, the value of R is positive in the upstream half and negative in the downstream half of the region where $q_1'^2$ is maximum. We indicate this region by a box in Fig. 11b. The first term in R , $-\overline{\mathbf{u}_1' q_1' \cdot \nabla \bar{q}_1}$, which represents the interaction between the bandpass eddies and time-mean flow, is shown in Fig. 11c. The zonal component

$-\overline{u_1' q_1' / \partial \bar{q}_1 / \partial x}$ of this term is negligible (not shown), and therefore the meridional component $-\overline{v_1' q_1' / \partial \bar{q}_1 / \partial y}$ is essentially the same as the sum (Fig. 11c). This term includes both local sources/sinks and advection of the bandpass enstrophy by the time-mean flow (Black and Dole 1993). The maximum of $-\overline{\mathbf{u}_1' q_1' \cdot \nabla \bar{q}_1}$ lies in the upstream half of the $q_1'^2$ maximum (Fig. 11a). The dominant negative contribution to R in the downstream half of the maximum $q_1'^2$ is the scale-selective horizontal diffusion $-\overline{\nu q_1' \nabla^8 q_1'}$ indicated by region B in Fig. 11d. In the same figure, there is another locally enhanced enstrophy dissipation region, denoted by C, 30 degrees downstream of the mountain. The regions B and C correspond to the jet entrance regions. The secondary jet entrance corresponding to region B can be seen in Fig. 2a. This secondary, weak jet streak can occur both due to reflection of the stationary wave at a turning point to the south and to the secondary stationary wave train

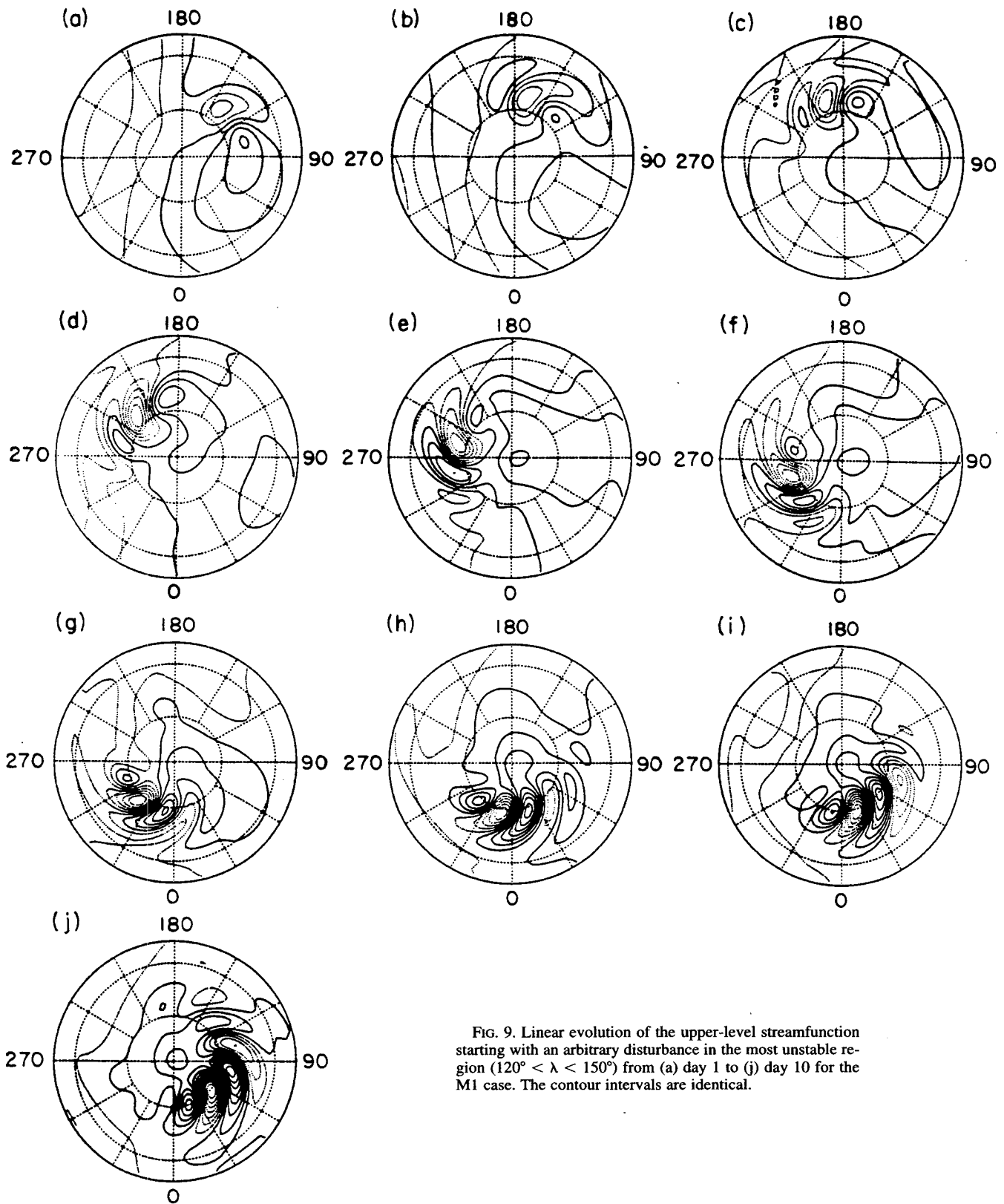


FIG. 9. Linear evolution of the upper-level streamfunction starting with an arbitrary disturbance in the most unstable region ($120^\circ < \lambda < 150^\circ$) from (a) day 1 to (j) day 10 for the M1 case. The contour intervals are identical.

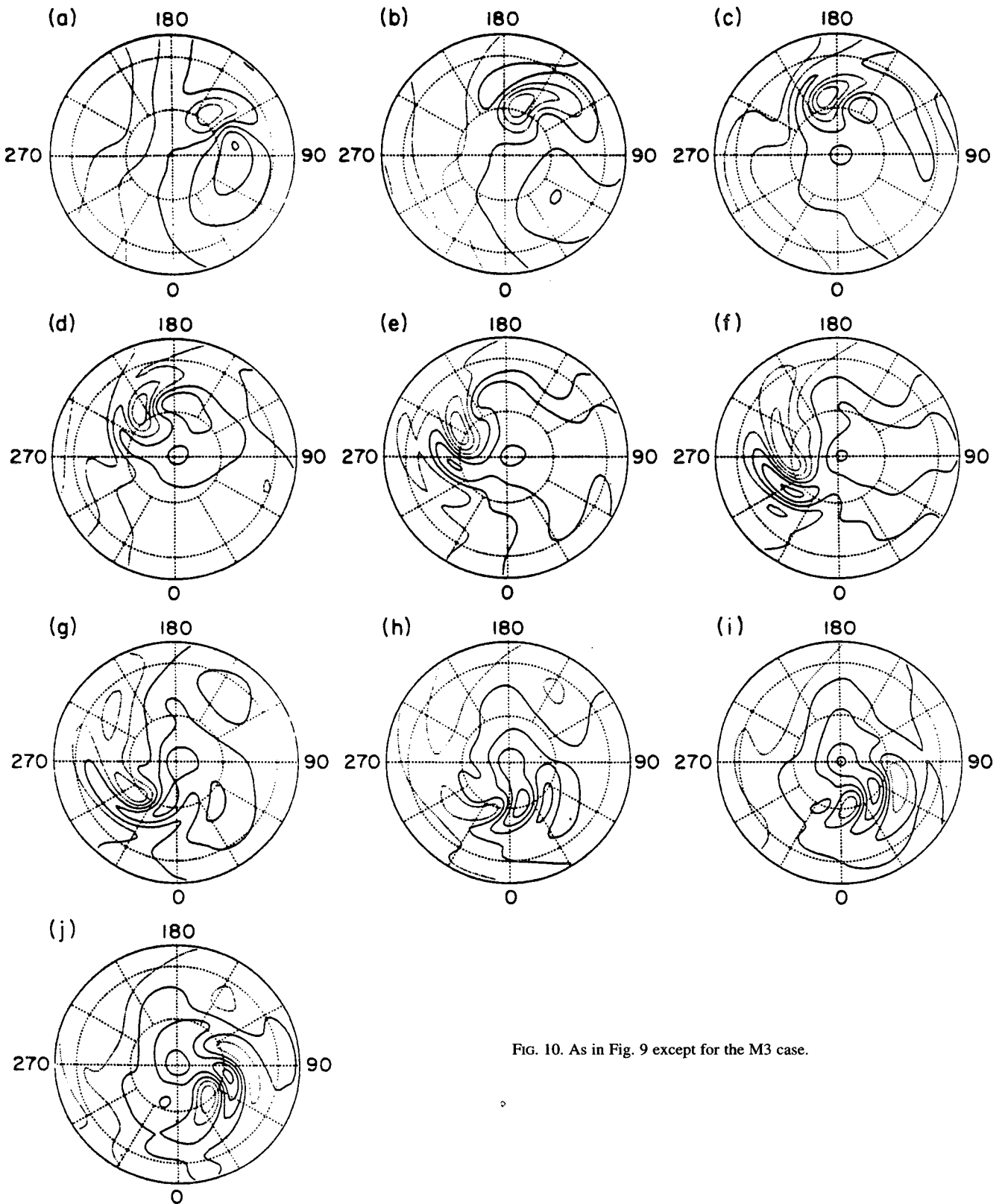
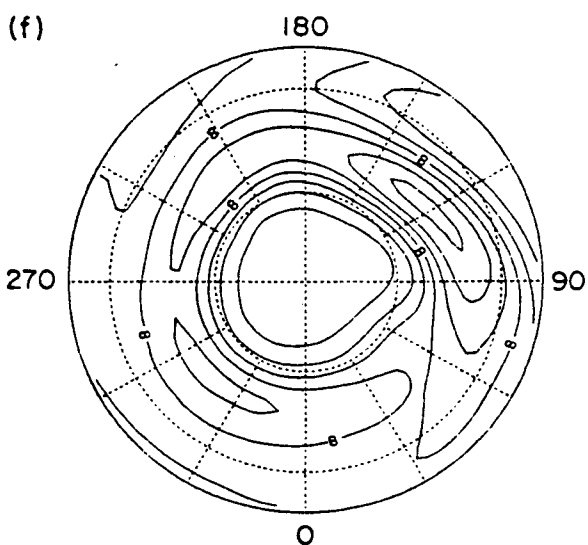
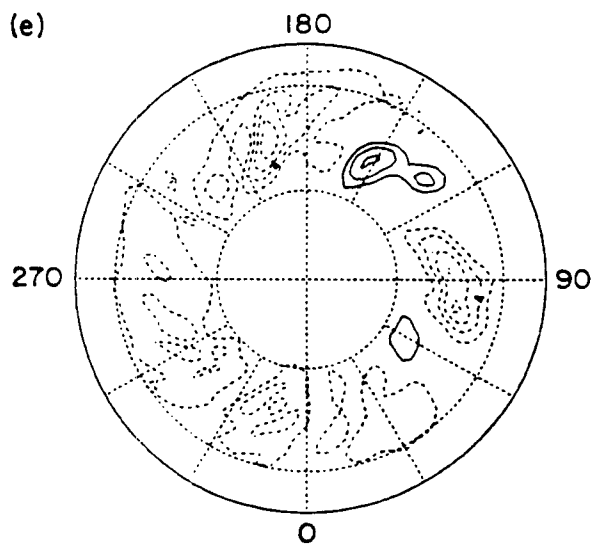
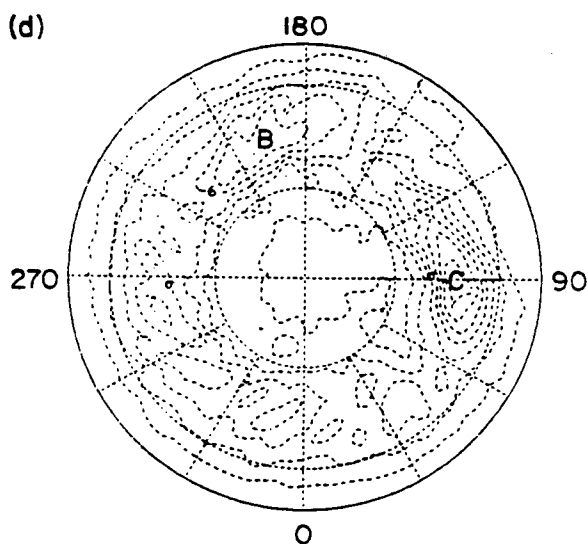
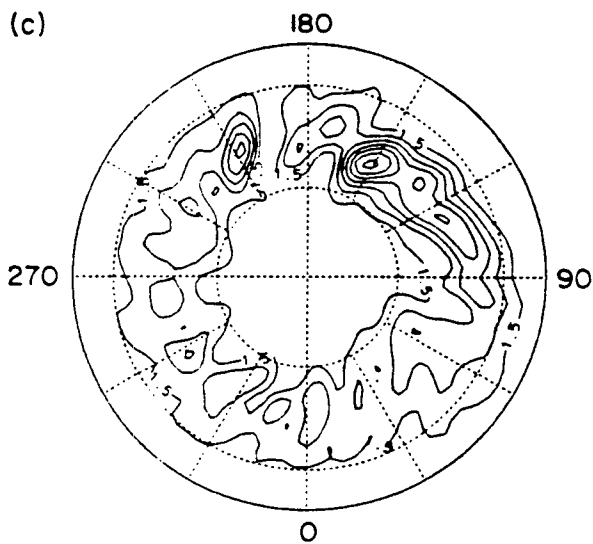
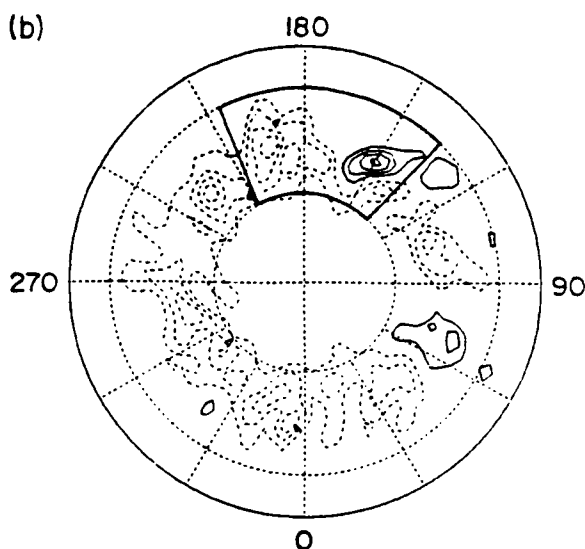
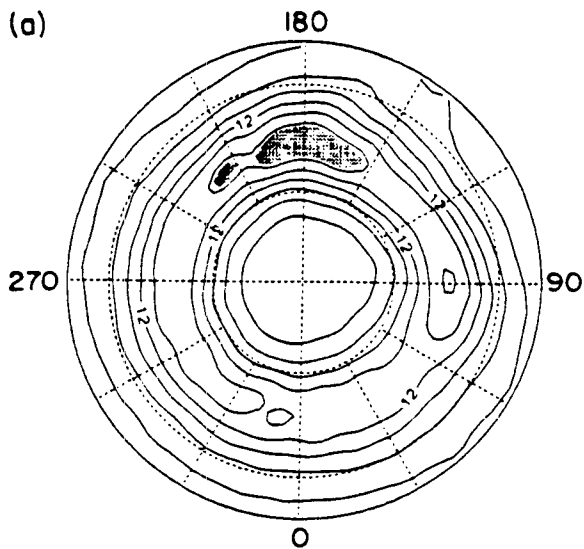


FIG. 10. As in Fig. 9 except for the M3 case.



emanating from the north of the mountain (Cook and Held 1992). Region C corresponds very well with a region of strong stretching deformation in the time-mean flow shown in Fig. 12. At B, unlike in nature's storm track, there is little deformation, yet there still is enhanced dissipation.

In these regions, the shearing deformation rate (not shown) is much smaller than that of the stretching deformation rate. It is fairly easy to identify a strong deformation region from the stationary zonal wind field as well, because the dominant contribution to the deformation field is the zonal variation of the zonal wind, $\partial U/\partial x$. Compared with the observed NH winter stationary wave (e.g., Fig. 13 of Blackmon et al. 1977), the deformation field (Fig. 12) in this model seems to be too weak overall, especially in the storm track region.

The sum of $\overline{u'_1 q'_1} \cdot \nabla \overline{q'_1}$ and $-\nu \overline{q'_1 \nabla^8 q'_1}$ is shown in Fig. 11e. Comparison between Figs. 11b and 11e clearly indicates that these two terms can explain most of the R structure. Therefore, at least in this model, the potential enstrophy dissipation due to the horizontal diffusion plays an important role in the termination of the storm track, defined by the local potential enstrophy maximum. In the lower layer, enstrophy dissipation by Ekman friction also plays a role in the termination of the storm track, but its strength is about 30% that of the dissipation due to the horizontal diffusion.

Because the scale-selective diffusion is a somewhat arbitrary parameterization, which is used to mimic the scales unresolved by the model, we examine the sensitivity of the enstrophy dissipation to the value of the diffusion coefficient. Once again, we integrate the M1 model for 4000 days with $\nu = 8 \times 10^{37}$ instead of 8×10^{38} . The results for this less diffusive case (not shown) are very similar to the more diffusive case, shown in Fig. 11, except for some minor changes such as a somewhat longer zonal extent of the storm track and rather noisy eddy statistics. The diffusive dissipation remains largely responsible for the termination of the storm track even if the diffusion coefficient is greatly reduced. Here we use the diffusive dissipation to measure the enstrophy cascade to small scales.

Observational (Lau 1979) and model studies (Kushnir and Esbensen 1986b; Sheng and Derome 1991) of the Northern Hemisphere showed that barotropic decay of the transient eddies occurs at the jet exit, and the growth and decay of the eddies in the storm track can be explained by baroclinic growth followed by barotropic decay. Dissipation by subgrid-scale diffusion and other frictional mechanisms, such as surface friction, has been ignored in those studies. Figure 13 shows eddy kinetic energy (EKE) and baroclinic and baro-

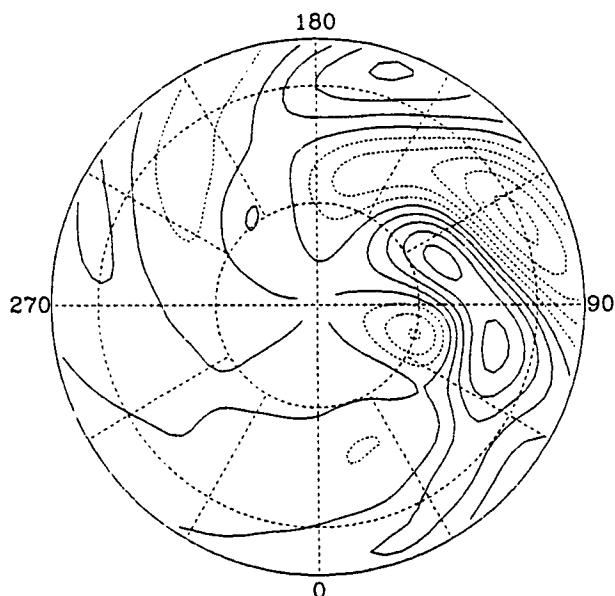
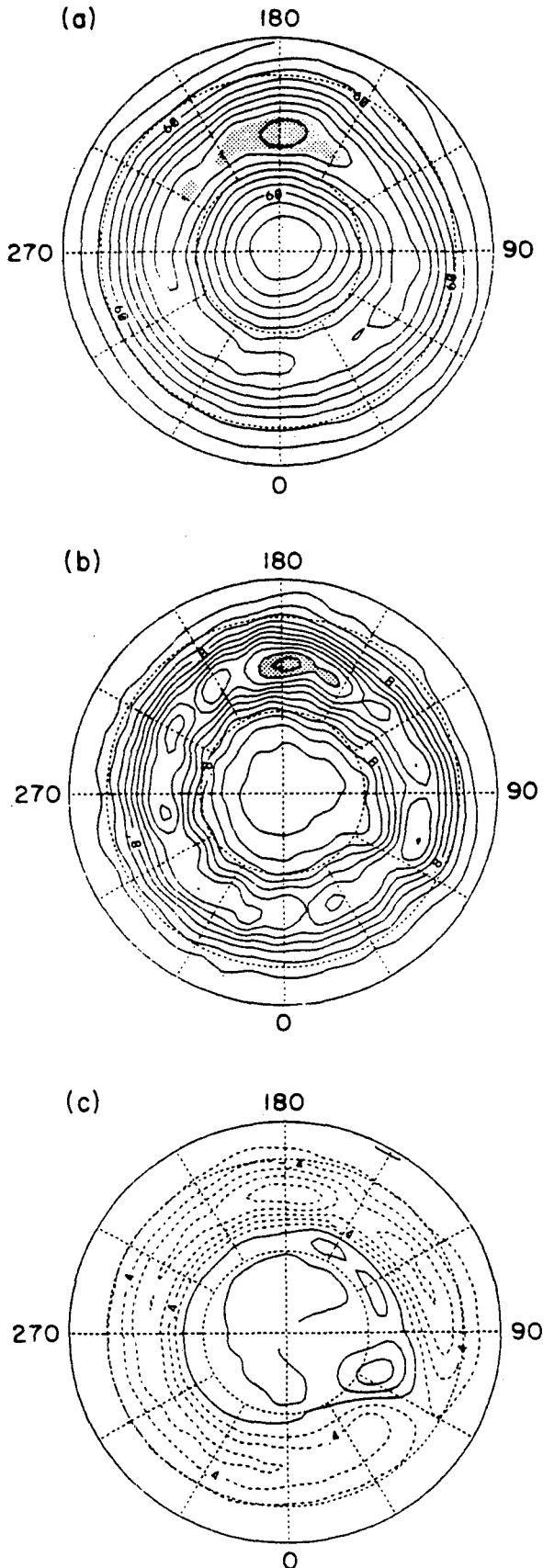


FIG. 12. Time-mean upper-level stretching deformation field for the M1 case. The contour interval is $1.5 \times 10^{-5} \text{ s}^{-1}$. Solid contours are positive and dashed contours are negative.

tropic energy conversion. (BC and BT, respectively). The maximum BC (Fig. 13b) occurs slightly upstream of the EKE maximum (Fig. 13a). The strongest barotropic conversion (Fig. 13c) lies slightly downstream and equatorward of the maximum EKE, with the structure of BT being more zonally symmetric than that of the observed Northern Hemisphere (Fig. 13 in Lau 1979). This zonally symmetric structure of BT resembles the Southern Hemisphere storm track (Trenberth 1982, 1991). Dissipation by subgrid-scale diffusion (not shown, but the structure is very similar to Fig. 11e) is also strongest downstream of the maximum EKE, with its magnitude being about the same as that of the negative barotropic conversion in that region. Dissipation of EKE by Ekman damping (not shown) also exhibits an essentially identical spatial structure to that by the diffusion, but with a smaller magnitude. At least in this model, dissipation of EKE by diffusion plays as equally important a role as that by the barotropic conversion in terminating the storm track. Since the potential vorticity flux combines both the momentum and the heat flux, in the potential enstrophy budget the distinction of BT and BC was not made.

One can also perform the potential enstrophy diagnostics for the unstable linear modes. Figure 14a shows upper-level RPEA potential enstrophy variance $\{q_1'^2\}$ of mode 1 for the M1 case. As in $\{\psi_1'^2\}$, the storm

FIG. 11. Bandpass eddy potential enstrophy budget for the M1 case. Upper-level (a) potential enstrophy, (b) R [see (15) in the text], (c) $-\overline{u'_1 q'_1} \cdot \nabla \overline{q'_1}$, (d) $-\nu \overline{q'_1 \nabla^8 q'_1}$, (e) $-\overline{u'_1 q'_1} \cdot \nabla \overline{q'_1} - \nu \overline{q'_1 \nabla^8 q'_1}$, and (f) time-mean meridional potential vorticity gradient. Contour intervals are (a) $3 \times 10^{-11} \text{ s}^{-3}$, (b) $2 \times 10^{-15} \text{ s}^{-3}$, (c) $1.5 \times 10^{-15} \text{ s}^{-3}$, (d) $1.5 \times 10^{-15} \text{ s}^{-3}$, (e) $2 \times 10^{-15} \text{ s}^{-3}$, and (f) $2 \times 10^{-10} \text{ m}^{-1} \text{ s}^{-1}$. Solid contours are positive, and dashed contours are negative.

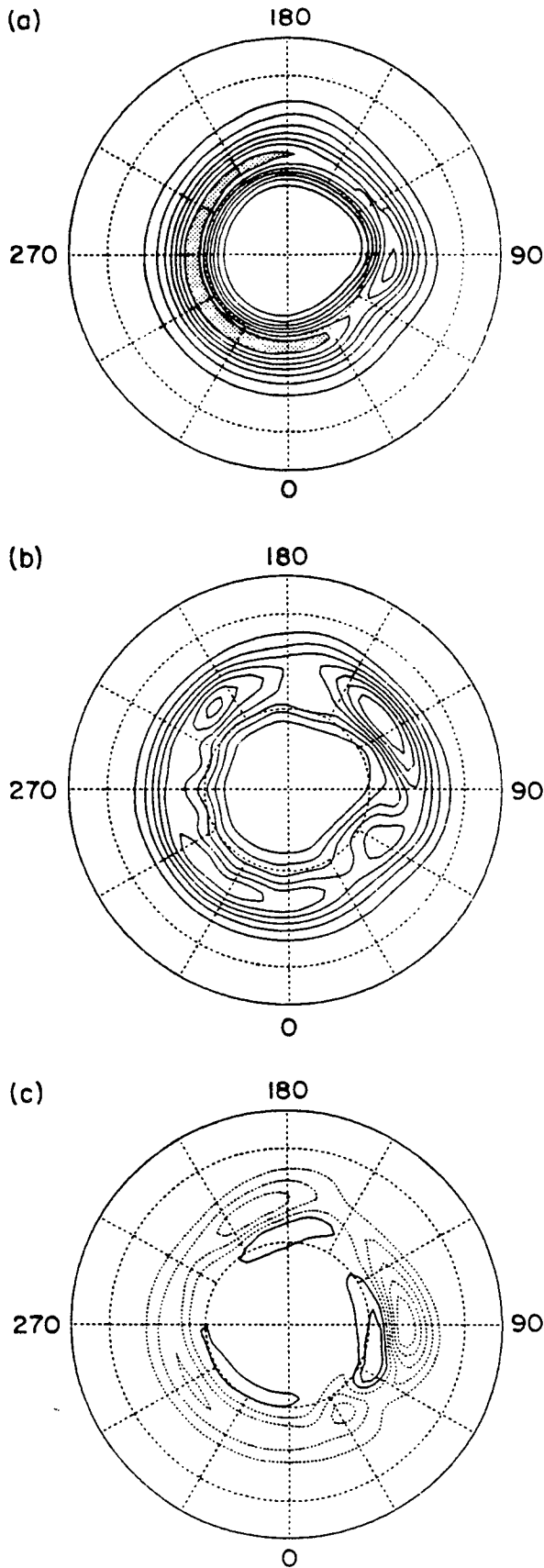


track as defined by the enstrophy variance extends farther downstream than that of the climatological storm track (Fig. 11a). Figure 14b shows that the large positive value of $-\{\mathbf{u}'_1 q'_1\} \cdot \nabla \bar{q}_1$ extends farther downstream than its nonlinear counterpart (Fig. 11c). The potential enstrophy dissipation by horizontal diffusion in this linear model is not strong enough to offset the positive value of $-\{\mathbf{u}'_1 q'_1\} \cdot \nabla \bar{q}_1$ except in the immediate vicinity of the mountain (Fig. 14c). This analysis indicates that there are at least two reasons for the difference between the nonlinear and linear storm tracks; in the linear model, 1) dissipation is too weak and 2) the interactions between the mean and eddies, $-\{\mathbf{u}'_1 q'_1\} \cdot \nabla \bar{q}_1$, are different.

Analysis of the potential enstrophy budget for the M3 case is more complicated than that for the M1 case. Figure 15a shows the eddy potential enstrophy at the upper level for the M3 case. While there is a reasonably good agreement between the M1 and M3 cases in terms of the location of the maximum eddy streamfunction amplitude and heat flux (see Figs. 4 and 5), the maximum $q_1'^2$ (at $\lambda = 200^\circ$) lies 30 degrees downstream of that for the M1 case (compare with Fig. 11a). Once again, there are three local maxima in the M3 case, and we refer to the particular maximum that has a counterpart in the M1 case. As shown in Fig. 15b, the value of R is positive in the upstream half and negative in the downstream half of the $q_1'^2$ maximum.

Both the meridional and zonal components of $-\mathbf{u}'_1 q'_1 \cdot \nabla \bar{q}_1$ are shown in Figs. 15c and 15d because the zonal component turns out to be important in the budget although the meridional component is stronger (note that the contour interval in Fig. 15c is three times greater than that in Fig. 15d). The maximum of $-\bar{v}'_1 q'_1 (\partial \bar{q}_1 / \partial y)$ (Fig. 15c) lies at $\lambda = 120^\circ$, whereas its counterpart in the M1 case (Fig. 11c) is at $\lambda = 150^\circ$. Also, the value of $-\bar{v}'_1 q'_1 (\partial \bar{q}_1 / \partial y)$ for the M3 case is 20% smaller than that for the M1 case. An explanation for these differences can be found in the structure of $\partial \bar{q}_1 / \partial y$; the distance between the $\partial \bar{q}_1 / \partial y$ minima and maxima is much shorter for the M3 case (Fig. 15g) than that for the M1 case (Fig. 11f). Therefore, the value of $-\bar{v}'_1 q'_1 (\partial \bar{q}_1 / \partial y)$ (Fig. 15c) cannot remain large except near the maximum $\partial \bar{q}_1 / \partial y$. The three maxima, $-\bar{u}'_1 q'_1 (\partial \bar{q}_1 / \partial x)$ (Fig. 15d), lie 10 degrees downstream of the corresponding mountain, very similar to the structure of $\partial \bar{q}_1 / \partial x$ (not shown). The scale-selective horizontal diffusion, $-\nu q_1' \nabla^2 q_1'$ (Fig. 15e), shows three regions of enhanced dissipation. Because the two enstrophy dissipation maxima in the M1 case, indicated by B and C in Fig. 11d, are nearly 120 de-

FIG. 13. Bandpass (a) eddy kinetic energy, (b) baroclinic energy conversion, and (c) barotropic energy conversion for the M1 case. The contour intervals are (a) $20 \text{ m}^2 \text{ s}^{-2}$, (b) $2 \times 10^{-4} \text{ m}^2 \text{ s}^{-3}$, and (c) $2 \times 10^{-4} \text{ m}^2 \text{ s}^{-3}$. Solid contours are positive and dashed contours are negative.



grees apart from each other, it is impossible to distinguish these two different regions in the M3 case.

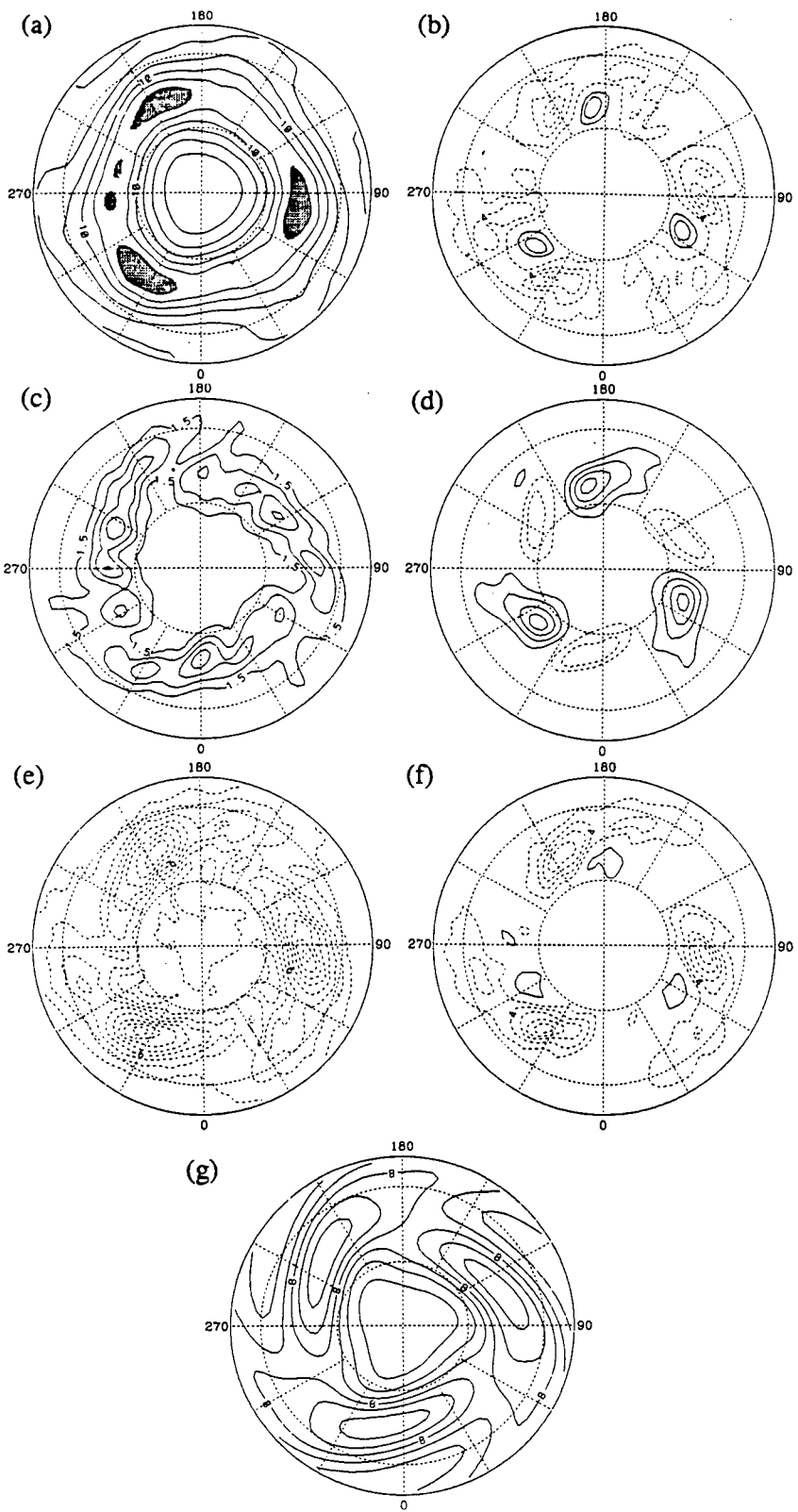
The sum of $-\overline{u'q'_1}(\partial\overline{q'_1}/\partial x)$, $-\overline{v'q'_1}(\partial\overline{q'_1}/\partial y)$, and $-\nu q'_1 \nabla^8 q'_1$ is shown in Fig. 11f. Although the dissipation dominates, the overall pattern agrees with R (Fig. 11b). It is clear that $-\overline{u'q'_1}(\partial\overline{q'_1}/\partial x)$ plays an important role in the regions of positive values for R . On the other hand, the positive contribution of $-\overline{v'q'_1}(\partial\overline{q'_1}/\partial y)$ is entirely offset by $-\nu q'_1 \nabla^8 q'_1$. This balance is quite different from that for the M1 case, and therefore it is not surprising that the location of the potential enstrophy maximum is different between the two cases.

Figure 16a shows the upper-level RPEA potential enstrophy variance $\{q'_1{}^2\}$ of mode 1 for the M3 case. As for the nonlinear case discussed above, the maximum $\{q'_1{}^2\}$ lies 30 degrees downstream of the corresponding maximum $\{\psi'_1{}^2\}$ (Fig. 8a). The sum of $-\{\mathbf{u}'q'_1\} \cdot \nabla \overline{q'_1}$ and the damping terms (thermal, Ekman, and diffusive dissipation) are shown in Fig. 16b with its regions of positive and negative values corresponding to upstream and downstream, respectively, of each maximum $\{q'_1{}^2\}$. Figure 16c and 16d show $-\{v'q'_1\}(\partial\overline{q'_1}/\partial y)$ and $-\{u'q'_1\}(\partial\overline{q'_1}/\partial x)$, respectively. Although the details are not the same, they resemble their nonlinear counterparts (Figs. 15c and 15d) reasonably well in terms of the location of their maxima. As shown in Fig. 16e, the scale-selective diffusion $-\nu\{q'_1 \nabla^8 q'_1\}$ depicts $-\nu q'_1 \nabla^8 q'_1$ quite well except for the regions with positive values north of the mountains. In contrast to the M1 case, the ratio of the maximum value of $-\nu\{q'_1 \nabla^8 q'_1\}$ to that of $-\{\mathbf{u}'q'_1\} \cdot \nabla \overline{q'_1}$ in the linear model is 1.5, and this is very close to the ratio (=1.8) of $-\nu q'_1 \nabla^8 q'_1$ to $-\mathbf{u}'q'_1 \cdot \nabla \overline{q'_1}$ in the nonlinear calculation.

The sum of $-\{\mathbf{u}'q'_1\} \cdot \nabla \overline{q'_1}$ ($= -\{v'q'_1\}(\partial\overline{q'_1}/\partial y) - \{u'q'_1\}(\partial\overline{q'_1}/\partial x)$) and $-\nu\{q'_1 \nabla^8 q'_1\}$ is shown in Fig. 16f, which captures the essence of Fig. 16b. Comparing Figs. 16c, 16d, 16e, and 16f, it is clear that the positive value of $-\{\mathbf{u}'q'_1\} \cdot \nabla \overline{q'_1}$ away from northeast of the mountains is offset by the negative value of $-\nu\{q'_1 \nabla^8 q'_1\}$, and once again the role of $-\{u'q'_1\}(\partial\overline{q'_1}/\partial x)$ is important for the local potential enstrophy maximum.

In summary, the potential enstrophy budget for the M3 case reveals striking similarity between the nonlinear and linear model, and the key reason for the good agreement between the climatological and the linear storm track is that the zonal wavelength of the stationary wave is sufficiently short that the large positive value of both $-\overline{v'q'_1}(\partial\overline{q'_1}/\partial y)$ and $-\{v'q'_1\}(\partial\overline{q'_1}/\partial y)$

FIG. 14. RPEA potential entropy budget in for the M1 case. Upper-level (a) potential entropy, (b) $-\{\mathbf{u}'q'_1\} \cdot \nabla \overline{q'_1}$, and (c) $-\nu\{q'_1 \nabla^8 q'_1\}$ of the most unstable mode (mode 1/R30). The contour interval in (b) is five times greater than that in (c). Solid contours are positive and dashed contours are negative.



cannot be maintained except near the small region of the maximum $\partial\bar{q}_1/\partial y$.

6. Discussion and concluding remarks

A two-level primitive equation (PE) model with idealized mountains is used to compare the linear storm track, as inferred from the unstable linear modes of the time-mean flow, with the model's climatological storm track. For the M1 case, the modes are convectively unstable, and the linear storm track measured by streamfunction, heat flux, and potential enstrophy extends farther downstream than the climatological storm track of the model. In addition, the potential enstrophy budget indicates that the larger zonal scale of the linear storm track is both due to its stronger potential enstrophy generation and to its weaker scale-selective dissipation in the linear model.

For the M3 case, both the potential enstrophy budget and various measures of storm tracks, such as eddy streamfunction and heat flux, show reasonably good agreement between the climatological and linear storm track. However, as in the M1 case, the most unstable mode is convectively unstable and is global. In Lin and Pierrehumbert (1993), it is argued that even if the linearly unstable mode is convectively unstable, it can grow appreciably as it propagates through the unstable region if the speed of propagation is small. As shown in Figs. 9 and 10, this process does not occur in either the M1 or M3 cases. In the M3 case the relative proximity of successive "unstable regions" makes the length of the periodic domain effectively small, and therefore one might expect that the global mode may take a shorter time to emerge than that for the M1 case. It is found, however, that it typically takes about 50 days for the global mode to emerge in both the M1 and M3 cases. We point out that a required time that a global mode to emerge from an arbitrary perturbation should depend on the properties of the background flow, such as the strength of the deformation and surface friction.

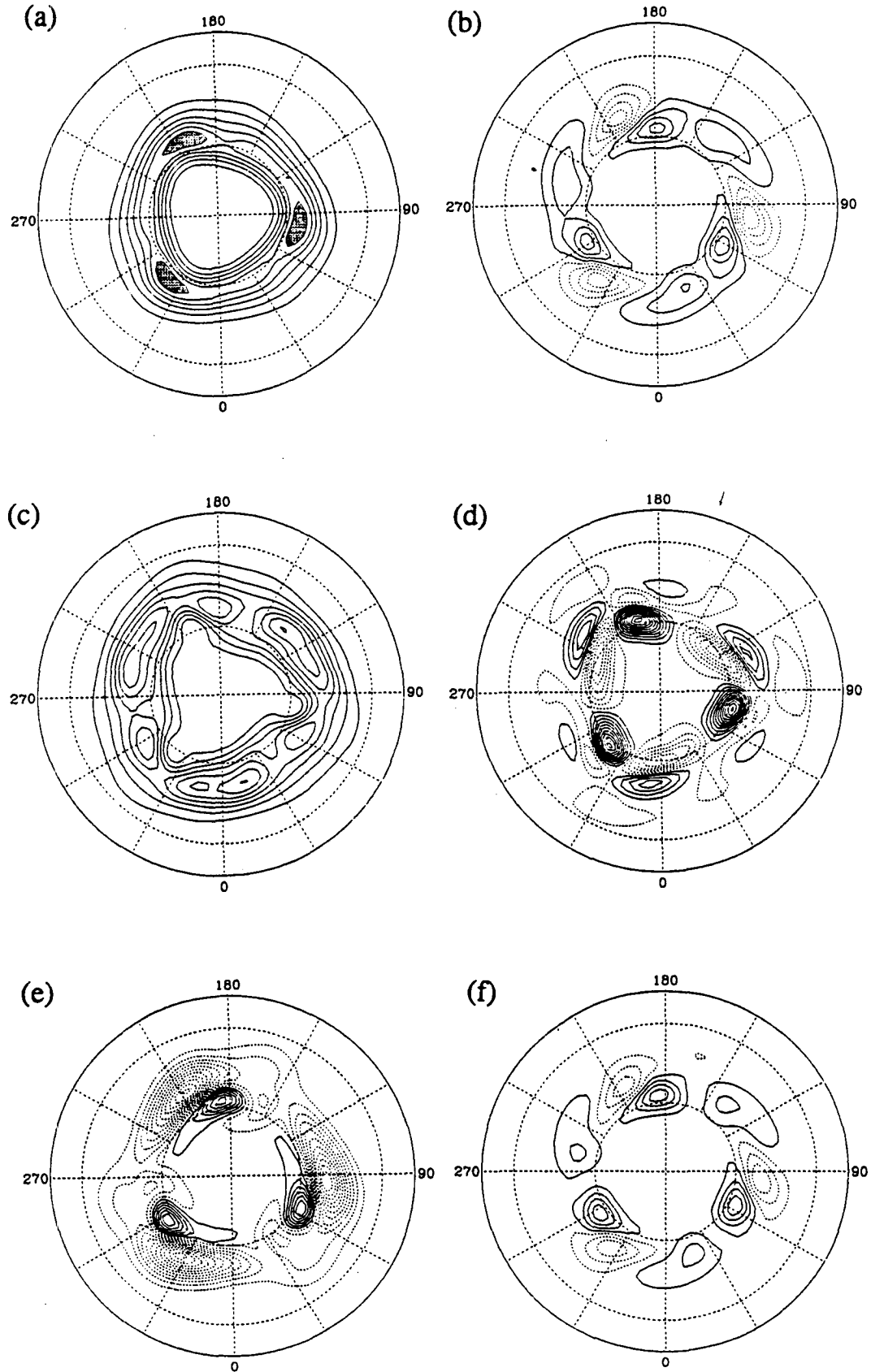
The M3 case shows that it is possible to obtain a linear mode that agrees reasonably well with the climatological storm track, even if the linear mode is convectively unstable and results from "recycling" of the wave activity. This means that the linear mode may look "right" for the wrong reason, and a mere "good agreement" between a linear mode and observations (or nonlinear model simulations) in terms of selected eddy statistics does not necessarily provide useful insight into the physical mechanism behind the storm tracks. In this study, the M1 case shows that when the stationary wavelength is sufficiently long, the convective

unstable linear mode is unable to capture the structure of the climatological storm track, illustrating that the reasonable agreement between the linear and climatological storm track for the M3 case can be fortuitous.

Although a global mode is unlikely to be relevant for the climatological storm track (Pierrehumbert 1984) due to the unrealistically long time required for the mode to evolve from an arbitrary perturbation, the way it gains a locally enhanced wave amplitude may be relevant for the atmosphere. Lee and Held (1993) found both with the present two-level model and in observations that the synoptic-scale baroclinic waves in the midlatitude atmosphere typically organize themselves into coherent wave packets. These packets often maintain their shape and speed as they propagate along a latitude circle. It is plausible then that the wave packet amplifies in certain geographical locations as it traverses through a stationary wave as the global mode does. Consistent with this conjecture, Higgins and Schubert (1993) showed strong evidence that both Pacific and Atlantic storm tracks are closely related with coherent wave packets in a GCM.

Using an idealized two-layer quasigeostrophic model, Pierrehumbert (1984) argued that the observed NH wintertime circulation is likely to support absolute instability for both Pacific and Atlantic storm tracks. Therefore, he speculates Frederiksen's (1983) result as a consequence of absolute instability. In the context of the two-layer model, the essential elements of a zonally varying flow of which the local instability is sought are the vertically averaged wind \bar{U} and the vertical wind shear DU defined as $\bar{U} = (U_1 + U_2)/2$ and $DU = U_1 - U_2$. Here, subscripts 1 and 2 refer to the upper and lower layer, respectively. To make use of two-layer results in observations, Pierrehumbert estimates DU as the difference between the 500-mb zonal wind in the jet core and the surface wind, and considers the surface wind to be essentially zero. This leads to $U = 0.5 DU$ at each point in the domain, and his WKB analysis (see Fig. 11 of Pierrehumbert 1984) gives a critical value of 0.725, which is the largest value of DU_{\min}/DU_{\max} that permits localization. Here, DU_{\min} and DU_{\max} are the minimum and maximum DU in the domain, respectively. However, if one estimates DU as the difference between the 250-mb and 750-mb wind in the jet core, $DU \approx U$ in the observed wintertime circulation (e.g., see Hoskins et al. 1989). Under this condition, the critical value is found to be 0.5, and the value of DU_{\min}/DU_{\max} is 0.45 for both Atlantic and Pacific zones where DU_{\min} is the first minimum in DU downstream of each region of maximum DU . Therefore,

FIG. 15. Bandpass eddy potential enstrophy budget for the M3 case. Upper-level (a) potential enstrophy, (b) R [see (15) in the text], (c) $-\bar{v}_1'q_1'(\partial\bar{q}_1/\partial y)$, (d) $-\bar{u}_1'q_1'(\partial\bar{q}_1/\partial x)$, (e) $-\nu q_1'\nabla^2 q_1'$, (f) $-\bar{\mathbf{u}}_1'q_1' \cdot \nabla \bar{q}_1' - \nu q_1'\nabla^2 q_1'$, and (g) time-mean meridional potential vorticity gradient. Contour intervals are (a) $3 \times 10^{-11} \text{ s}^{-3}$, (b) $2 \times 10^{-15} \text{ s}^{-3}$, (c) $1.5 \times 10^{-15} \text{ s}^{-3}$, (d) $0.5 \times 10^{-15} \text{ s}^3$, (e) $1.5 \times 10^{-15} \text{ s}^{-3}$, (f) $2 \times 10^{-15} \text{ s}^{-3}$, and (g) $2 \times 10^{-10} \text{ m}^{-1} \text{ s}^{-1}$. Solid contours are positive and dashed contours are negative.



the two zones in the wintertime flow barely meet the localization criterion.

Returning to the experiments presented here, the value of DU_{\min}/DU_{\max} in the time-mean flow for the M1 and M3 cases are 0.66 and 0.75, respectively. These are well above the critical value of 0.5; thus, absolute instability is absent in both cases. Indeed, the initial growth of a small disturbance originating at the maximum baroclinicity region clearly indicates that the time-mean flows for both the M1 and the M3 cases only support convectively unstable linear modes.

To this end, we note that the two-level PE model used in this study produces a rather strong lower-level zonal wind speed ($\sim 16 \text{ m s}^{-1}$) compared with the observed wind speeds ($\sim 10 \text{ m s}^{-1}$ at 750 mb). When surface friction is increased in an attempt to reduce the wind speed, the circulation evolves into a superrotating state (Saravanan 1993). We also varied the meridional temperature gradient to achieve a desirable ratio of vertical wind shear to the vertically averaged wind, but it was unsuccessful: the increased meridional temperature gradient increases the lower-level wind speed as well as the upper-level wind speed, and therefore to keep the lower-level wind speed smaller, one needs to increase the surface friction. But once again this results in a superrotating state. Since the ratio of the vertical wind shear to the vertically averaged wind is a crucial factor for the existence of local modes (Pierrehumbert 1984), the strong lower-level wind in this two-level model may exaggerate the effect of convective instability. It would be useful to examine the linear instability of the stationary waves found in a GCM or in a model with higher vertical resolution with idealized mountains, because the rather strong lower-level wind in the two-level model may be solely responsible for the convective instability of the model atmosphere.

We also point out that the location of the storm track measured by the eddy streamfunction amplitude can be very different from that measured by the eddy potential enstrophy. This is illustrated in the M3 case where the eddy potential enstrophy maximum lies 90 degrees upstream of the eddy streamfunction maximum while the two maxima lie nearly at the same location in the M1 case. We suspect that the sensitivity of the location of the storm track to the choice of variable is due to the horizontally varying structure and scale of the waves. As the potential enstrophy budget indicates, the dynamics involving the potential enstrophy maximum in the M1 case is different from that of the M3 case, yet the streamfunction amplitude does not discriminate this difference between the two cases. This type of sensitivity can also be seen in the observations. In Fig. 5a

of Plumb (1986), the bandpass eddy potential enstrophy at 500 mb shows its Pacific storm track just north-east of Japan, whereas the bandpass eddy kinetic energy (Fig. 5 of Blackmon et al. 1977) at the same level shows the center of the Pacific storm track 20 degrees downstream of the date line.

In studies involving energetics of the transient eddies, barotropic decay has long been recognized as a mechanism whereby the transient eddies lose energy to the mean flow downstream of the jet (Lau 1979; Kushnir and Esbensen 1986b). In particular, it is shown that the transient eddies are meridionally elongated downstream of the storm track, and this is responsible for the barotropic decay in that region [$(v'^2 - u'^2)\partial\bar{U}/\partial x < 0$, together with $-u'v'\partial\bar{U}/\partial y < 0$]. Meridional elongation of the eddy in this region is consistent with the idea of the eddy straining mechanism in a diffluent jet region (Shutts 1983), and one may expect a subsequent cascade of enstrophy to small scales. Therefore, it may be that the barotropic decay in the downstream half of the storm track is intimately related with the dissipation of the eddies in that region.

As mentioned in section 2, we point out that the idealized model that we use in this study lacks several physical features that can play an important role in storm track dynamics of the atmosphere. For example, the absence of diabatic heating, zonally varying surface friction, and static stability due to land-sea contrast, which are shown to be important in localization of storm tracks (Hoskins and Valdes 1990; Chang and Orlanski 1993; Mak 1993; Whitaker and Barcilon 1992) almost certainly exaggerates the effect of the enstrophy dissipation in terminating the storm track in our model. The reason for the minor role of surface friction in dissipating wave activity at the downstream end of the storm tracks may be because of both weak surface friction and lack of diabatic heating. Therefore, we emphasize that our result simply illustrates a possible mechanism that may be relevant for the storm track's termination, at least in the upper troposphere. In light of the results of recent idealized model studies, for the diagnosis of the storm tracks in either observations or in realistic models such as GCMs, it would be useful to investigate the effect of wave dissipation in more detail.

Acknowledgments. The author would like to thank to Drs. G. W. Branstater, S. B. Feldstein, and J. Tribbia for their suggestions and comments on this work. Part of this work was initiated from the author's Ph. D. dissertation. This manuscript also benefited from comments by two anonymous reviewers.

FIG. 16. RPEA potential enstrophy budget for the M3 case. Upper-level (a) potential enstrophy; (b) the sum of thermal, Ekman, diffusive dissipation, and $-\{u'q'\} \cdot \nabla \bar{q}$; (c) $-\{v'q'\}(\partial \bar{q}/\partial y)$; (d) $-\{u'q'\}(\partial \bar{q}/\partial x)$; (e) $-\nu\{q'\nabla^2 q'\}$; and (f) $-\{u'q'\} \cdot \nabla \bar{q} - \nu\{q'\nabla^2 q'\}$ of the most unstable mode (mode 1/R30). The same contour interval is used in (b) and (f), and (c) and (e). The contour interval in (d) is three times greater than that in (c) and (e). Solid contours are positive and dashed contours are negative.

REFERENCES

- Black, R. B., and R. M. Dole, 1993: The dynamics of large-scale cyclogenesis over the North Pacific Ocean. *J. Atmos. Sci.*, **50**, 421–442.
- Blackmon, M. L., J. M. Wallace, N.-C. Lau, and S. L. Mullen, 1977: An observational study of the Northern Hemisphere wintertime circulations. *J. Atmos. Sci.*, **34**, 1040–1053.
- Chang, K. M., and I. Orlanski, 1993: On the dynamics of a storm track. *J. Atmos. Sci.*, **50**, 1413–1428.
- Cook, K. H., and I. M. Held, 1992: The stationary response to large-scale orography in a general circulation model and a linear model. *J. Atmos. Sci.*, **49**, 525–539.
- Dole, R. M., 1986: Persistent anomalies of the extratropical Northern Hemisphere wintertime circulation: Structure. *Mon. Wea. Rev.*, **114**, 178–207.
- Feldstein, S. B., and I. M. Held, 1989: Barotropic decay of baroclinic waves in a two-layer beta-plane model. *J. Atmos. Sci.*, **46**, 3416–3430.
- Frederiksen, C. S., and J. S. Frederiksen, 1992: Northern Hemisphere storm tracks and teleconnection patterns in primitive equation and quasigeostrophic models. *J. Atmos. Sci.*, **49**, 1443–1458.
- Frederiksen, J. S., 1979a: The effect of long planetary waves on the regions of cyclogenesis: Linear theory. *J. Atmos. Sci.*, **36**, 195–204.
- , 1979b: Baroclinic instability of zonal flows and planetary waves in multi-level models on a sphere. *J. Atmos. Sci.*, **36**, 2320–2335.
- , 1983: Disturbance and eddy fluxes in Northern Hemisphere flows: Instability of three-dimensional January and July flows. *J. Atmos. Sci.*, **40**, 836–855.
- , and R. C. Bell, 1987: Teleconnection patterns and the roles of baroclinic, barotropic and topographic instability. *J. Atmos. Sci.*, **44**, 2200–2218.
- Hendon, H. H., 1986: Time-mean flow and variability in a nonlinear model of the atmosphere with orographic forcing. *J. Atmos. Sci.*, **43**, 433–448.
- Higgins, R. W., and S. D. Schubert, 1993: Low-frequency synoptic-eddy activity in the Pacific storm track. *J. Atmos. Sci.*, **50**, 1672–1690.
- Hoskins, B. J., and P. J. Valdes, 1990: On the existence of storm tracks. *J. Atmos. Sci.*, **47**, 1854–1864.
- , H. H. Hsu, I. N. James, M. Masutani, P. D. Sardeshmukh, and G. H. White, 1989: Diagnostics of the global atmospheric circulation based on ECMWF analyses 1979–1989. WCP-27, WMO, 217 pp.
- Kushnir, Y., and S. K. Esbensen, 1986a: Northern Hemisphere wintertime variability in a two-level general circulation model. Part I: General description. *J. Atmos. Sci.*, **43**, 2968–2984.
- , and ———, 1986b: Northern Hemisphere wintertime variability in a two-level general circulation model. Part II: The maintenance of short and long time-scale disturbances. *J. Atmos. Sci.*, **43**, 2985–2998.
- Lau, N.-C., 1979: The structure and energetics of transient disturbances in the Northern Hemisphere wintertime circulation. *J. Atmos. Sci.*, **36**, 982–995.
- , 1988: Variability of the observed midlatitude storm tracks in relation to low-frequency changes in the circulation pattern. *J. Atmos. Sci.*, **45**, 2718–2743.
- Lee, S., and I. M. Held, 1993: Baroclinic wave packets in models and observations. *J. Atmos. Sci.*, **50**, 1413–1428.
- Lin, S.-J., and R. T. Pierrehumbert, 1993: Is the midlatitude zonal flow absolutely unstable? *J. Atmos. Sci.*, **50**, 505–517.
- Mak, M., 1993: Local baroclinic instability induced by inhomogeneous stratification. *J. Atmos. Sci.*, **50**, 1629–1642.
- Mullen, S. L., 1987: Transient eddy forcing of blocking flows. *J. Atmos. Sci.*, **44**, 3–22.
- Pattersen, S., and S. J. Smebye, 1971: On the development of extratropical cyclones. *Quart. J. Roy. Meteor. Soc.*, **97**, 457–482.
- Pierrehumbert, R. T., 1984: Local and global baroclinic instability of zonally varying flow. *J. Atmos. Sci.*, **41**, 2141–2162.
- , 1986: Spatially amplifying modes of the Charney baroclinic instability problem. *J. Fluid Mech.*, **170**, 393–317.
- Plumb, R. A., 1986: Three-dimensional propagation of transient quasi-geostrophic eddies and its relationship with the eddy forcing of the time-mean flow. *J. Atmos. Sci.*, **43**, 1657–1678.
- Randel, W. J., and J. L. Stanford, 1985: The observed life cycle of a baroclinic instability. *J. Atmos. Sci.*, **42**, 1364–1373.
- Robertson, A. W., and W. Metz, 1989: Three-dimensional linear instability of persistent anomalous large-scale flows. *J. Atmos. Sci.*, **46**, 2783–2801.
- Saravanan, R., 1993: Equatorial superrotation and maintenance of the general circulation in two-level models. *J. Atmos. Sci.*, **50**, 1211–1227.
- Sheng, J., and J. Derome, 1991: On the interactions among flow components in different frequency bands in the Canadian Climate Centre general circulation model. *Atmos.–Ocean*, **29**, 62–84.
- Shutts, G. J., 1983: The propagation of eddies in diffluent jetstreams: Eddy vorticity forcing of ‘blocking’ flow fields. *Quart. J. Roy. Meteor. Soc.*, **109**, 737–761.
- Simmons, A. J., and B. J. Hoskins, 1978: The life cycles of some nonlinear baroclinic waves. *J. Atmos. Sci.*, **35**, 414–432.
- Trenberth, K. E., 1982: Seasonality in Southern Hemisphere eddy statistics at 500 mb. *J. Atmos. Sci.*, **39**, 2507–2520.
- , 1991: Storm tracks in the Southern Hemisphere. *J. Atmos. Sci.*, **48**, 2159–2178.
- Whitaker, J. S., and A. Barcilon, 1992: Type B cyclogenesis in a zonally varying flow. *J. Atmos. Sci.*, **49**, 1877–1892.